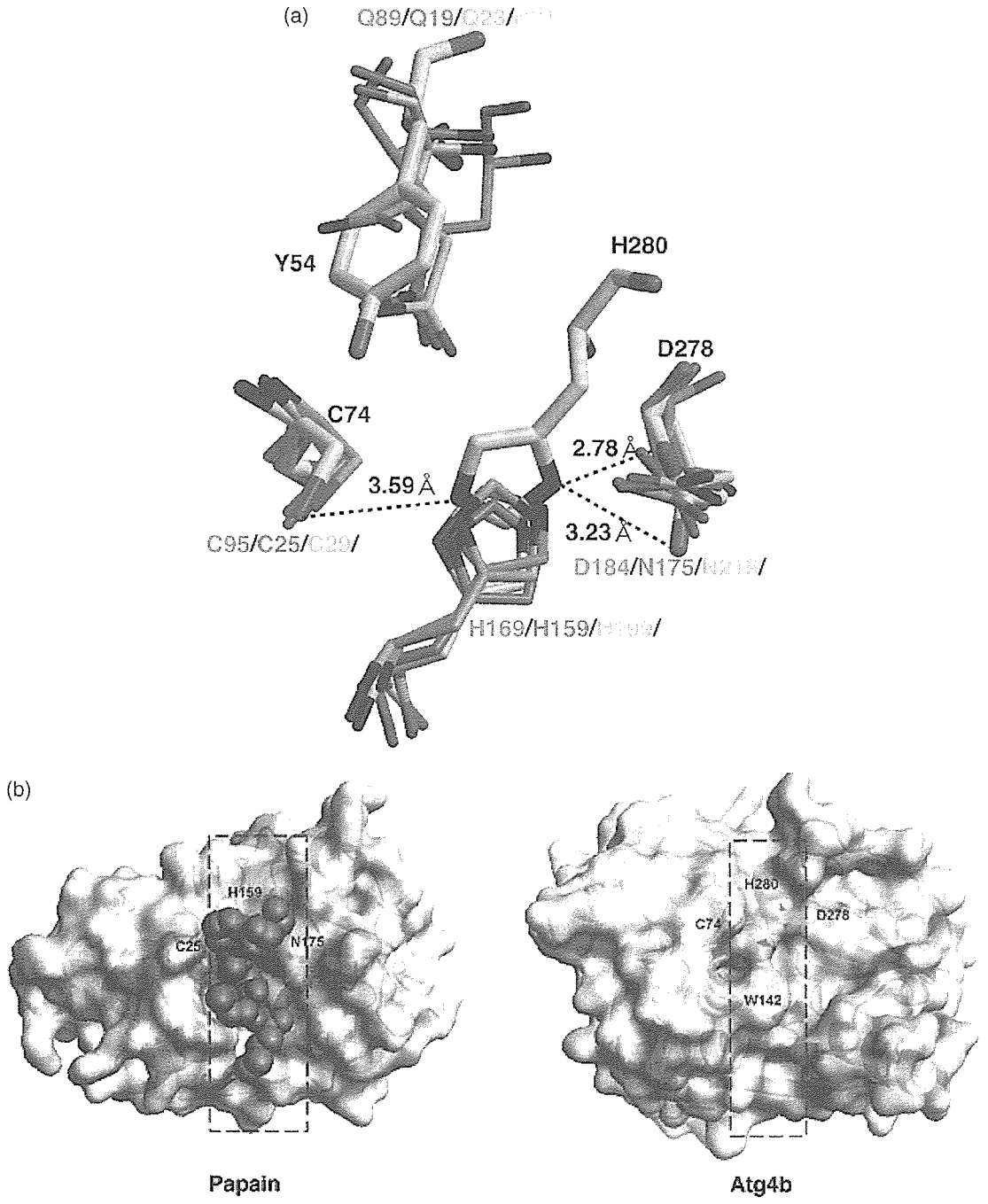

Figure 2. Comparison of the active sites among Atg4b and papain-like proteases. Active site residues of Atg4b, Y54, C74, D278 and H280 are shown as yellow stick models. Those of four papain-like cysteine proteases appear in cyan (UCH-L3: PDB ID code 1xd3), magenta (papain: PDB ID code 1pop), gold (cathepsin B: PDB ID code 1ito) and salmon (UBP: PDB ID code 1nbf). The Figure was prepared by superposition of UCH-L3, papain, cathepsin B and UBP on Atg4b. (b) Surface representation of papain complex with the N-terminal region of stefin B (PDB ID code 1stf)[25] and Atg4b. Protein surfaces are colored gray. The wavy line surrounds active site clefts. Bound stefin B is in red. The active site residues are in magenta.

a consequence of crystal packing. It is conceivable that the lid loop undergoes conformational change to an open form upon substrate binding.

Substrate recognition

Next, we conducted site-directed mutagenesis to change key residues assumed to participate in catalysis and substrate recognition of Atg4b. To investigate the processing activation of Atg4b against two Atg4b substrates, LC3 and GABARAP, *in vitro*, recombinant Atg4b proteins expressed in *Escherichia coli* were purified to homogeneity. As substrates, the C-terminal Myc-tagged LC3 (LC3-Myc) and GABARAP (GABARAP-Myc) were expressed in *E. coli* and purified to homogeneity.

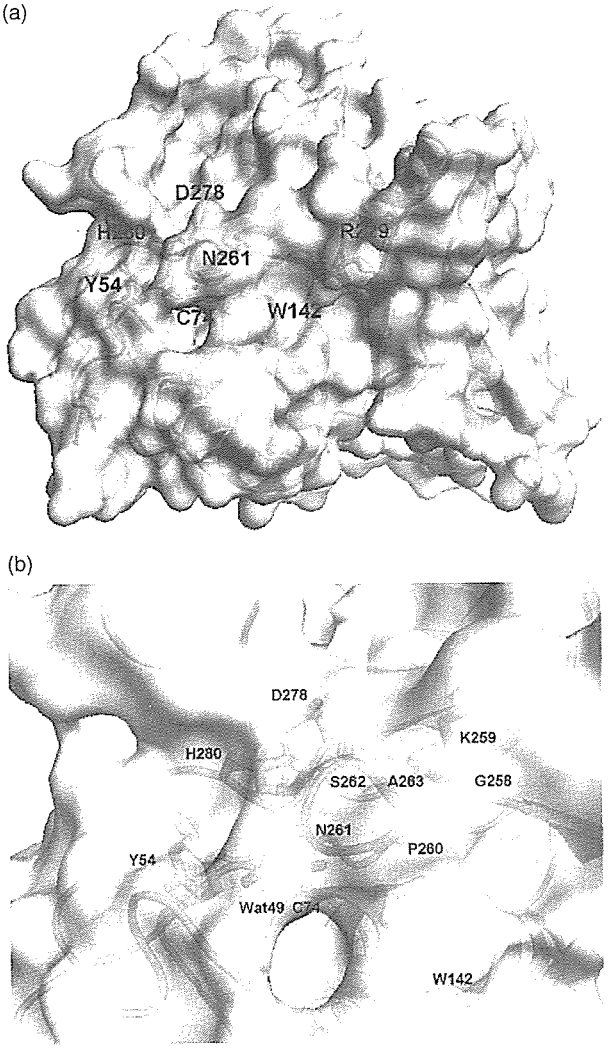

Figure 3. (a) Surface representation of Atg4b. The active site and the proposed substrate recognizing residues are individually labeled. (b) Clipping of the active site, Y54, C74, W142, D278 and H280, is shown in ball-and-stick representation. The red sphere is a water molecule. The lid loop (residues 258–263) covers the active site.

Incubation of each substrate with Atg4b released the Myc-tag, resulting in LC3 and GABARAP products, respectively, that migrated firstly in SDS-PAGE. For each mutant of Atg4b, the extent of the cleavage was determined by scanning Coomassie blue-stain (Supplementary Data, Figure S1a). Wild-type Atg4b cleaved both substrates. As expected, mutation of cysteine-74, one of the residues that comprises the catalytic triad was associated with a complete disappearance of the processing activity. Mutation of other residues comprising the catalytic triad also resulted in the loss of activity (data not shown). Since the crystal structures of LC3 and GABARAP were determined,[22,23] we built the model of the LC3 or GABARAP and Atg4b complex manually to predict key residues of Atg4b for substrate recognition. The interactions between the Ubl modifier, NEDD8 and its specific cysteine protease, NEDP1 also provided useful information.[24] Thus, W142 of Atg4b was predicted to form a π-stacking with F119 of LC3 and Y115 of GABARAP, which immediately precedes Gly. In addition, R229 of Atg4b was predicted to form a hydrogen bond with Q116 of LC3 and a salt-bridge with E112 of GABARAP. These appear to be key interactions, as neither the W142A nor R229A versions of Atg4b showed severe reduction of the protease activity.

While the assay employed the measures described above the processing activity of Atg4b *in vitro* it was also important to assay the de-conjugating activity of the protease. Using our recently developed *in vitro* reconstitution systems (Y.S., I. T., M.K., T.U. & E.K., unpublished results), we generated PE-conjugating LC3 and GABARAP (Supplementary Data, Figure S1b). The modified substrates migrated first compared with the un-modified substrates. Incubation of each substrate with Atg4b released PE, resulting in LC3 and GABARAP products, respectively, which migrated slowly in SDS-PAGE. For each mutant, the extent of cleavage was determined by immunoblotting with anti-LC3 and anti-GABARAP, respectively (Supplementary Data, Figure S1b). When the wild-type Atg4b was mixed with the substrates, both modified substrates were completely delipidated. Mutants with reduced activity, as demonstrated in the processing assay, were also defective in the de-conjugating assay. These results indicate that W142 and R229 residues in Atg4b are essential for recognition of both lipidated and native substrates.

In conclusion, we have demonstrated here that Atg4b is an endopeptidase with a unique high specificity toward Atg8 homologues, such as LC3 and GABARAP. Analysis of the crystal structure of the human Atg4b showed a catalytic mechanism similar to the papain superfamily cysteine proteinases. The mode of interaction between Atg4b and Atg8 homologues may be determined in the future by their co-crystallization.

Protein Data Bank accession code

The coordinates and structure factors have been deposited in the RCSB PDB (accession code 2D1I).

Acknowledgements

We thank all members of the BL44XU for their help in data collection at SPring-8. This work was supported by Grants-in-Aid for Scientific Research on Priority Area (C) from the Ministry of Education, Culture, Science and Technology of Japan.

Supplementary Data

Supplementary data associated with this article can be found, in the online version, at doi:10.1016/j.jmb.2005.11.018

References

1. Jentsch, S. & Pyrowolakis, G. (2000). Ubiquitin and its kin: how close are the family ties? *Trends Cell Biol.* **10**, 335–342.
2. Pickart, C. M. & Eddins, M. J. (2004). Ubiquitin: structures, functions, mechanisms. *Biochim. Biophys. Acta*, **1695**, 55–72.
3. Welchman, R. L., Gordon, C. & Mayer, R. J. (2005). Ubiquitin and ubiquitin-like proteins as multifunctional signals. *Nature Rev. Mol. Cell Biol.* **6**, 599–609.
4. Finley, D., Bartel, B. & Varshavsky, A. (1989). The tails of ubiquitin precursors are ribosomal proteins whose fusion to ubiquitin facilitates ribosome biogenesis. *Nature*, **338**, 394–401.
5. Wiborg, O., Pedersen, M. S., Wind, A., Berglund, L. E., Marcker, K. A. & Vuust, J. (1985). The human ubiquitin multigene family: some genes contain multiple directly repeated ubiquitin coding sequences. *EMBO J.* **4**, 755–759.
6. Schwartz, D. C. & Hochstrasser, M. (2003). A superfamily of protein tags: ubiquitin, SUMO and related modifiers. *Trends Biochem. Sci.* **28**, 321–328.
7. Kim, J. H., Park, K. C., Chung, S. S., Bang, O. & Chung, C. H. (2003). Deubiquitinating enzymes as cellular regulators. *J. Biochem. (Tokyo)*, **134**, 9–18.
8. Kabeya, Y., Mizushima, N., Yamamoto, A., Oshitani-Okamoto, S., Ohsumi, Y. & Yoshimori, T. (2004). LC3, GABARA and GATE16 localize to autophagosomal membrane depending on form-II formation. *J. Cell Sci.* **117**, 2805–2812.
9. Tanida, I., Sou, Y. S., Ezaki, J., Minematsu-Ikeguchi, N., Ueno, T. & Kominami, E. (2004). HsAtg4B/HsApg4B/autophagin-1 cleaves the carboxyl termini of three human Atg8 homologues and delipidates microtubule-associated protein light chain 3- and GABAA receptor-associated protein-phospholipid conjugates. *J. Biol. Chem.* **279**, 36268–36276.
10. Ichimura, Y., Kirisako, T., Takao, T., Satomi, Y., Shimonishi, Y., Ishihara, N. *et al.* (2000). A ubiquitin-like system mediates protein lipidation. *Nature*, **408**, 488–492.
11. Klionsky, D. J. (2005). The molecular machinery of autophagy: unanswered questions. *J. Cell Sci*, **118**, 7–18.
12. Ohsumi, Y. (2001). Molecular dissection of autophagy: two ubiquitin-like systems. *Nature Rev. Mol. Cell Biol.* **2**, 211–216.
13. Mizushima, N., Ohsumi, Y. & Yoshimori, T. (2002). Autophagosome formation in mammalian cells. *Cell Struct. Funct.* **27**, 421–429.
14. Kabeya, Y., Mizushima, N., Ueno, T., Yamamoto, A., Kirisako, T., Noda, T. *et al.* (2000). LC3, a mammalian homologue of yeast Apg8p, is localized in autophagosome membranes after processing. *EMBO J.* **19**, 5720–5728.
15. Holm, L. & Sander, C. (1993). Protein structure comparison by alignment of distance matrices. *J. Mol. Biol.* **233**, 123–138.
16. Wenig, K., Chatwell, L., von Pawel-Rammingen, U., Bjorck, L., Huber, R. & Sondermann, P. (2004). Structure of the streptococcal endopeptidase IdeS, a cysteine proteinase with strict specificity for IgG. *Proc. Natl Acad. Sci. USA*, **101**, 17371–17376.
17. Kirisako, T., Ichimura, Y., Okada, H., Kabeya, Y., Mizushima, N., Yoshimori, T. *et al.* (2000). The reversible modification regulates the membrane-binding state of Apg8/Aut7 essential for autophagy and the cytoplasm to vacuole targeting pathway. *J. Cell Biol.* **151**, 263–276.
18. Johnston, S. C., Larsen, C. N., Cook, W. J., Wilkinson, K. D. & Hill, C. P. (1997). Crystal structure of a deubiquitinating enzyme (human UCH-L3) at 1.8 Å resolution. *EMBO J.* **16**, 3787–3796.
19. Schroder, E., Phillips, C., Garman, E., Harlos, K. & Crawford, C. (1993). X-ray crystallographic structure of a papain–leupeptin complex. *FEBS Letters*, **315**, 38–42.
20. Yamamoto, A., Tomoo, K., Matsugi, K., Hara, T., In, Y., Murata, M. *et al.* (2002). Structural basis for development of cathepsin B-specific noncovalent-type inhibitor: crystal structure of cathepsin B-E64c complex. *Biochim. Biophys. Acta*, **1597**, 244–251.
21. Hu, M., Li, P., Li, M., Li, W., Yao, T., Wu, J. W. *et al.* (2002). Crystal structure of a UBP-family deubiquitinating enzyme in isolation and in complex with ubiquitin aldehyde. *Cell*, **111**, 1041–1054.
22. Sugawara, K., Suzuki, N. N., Fujioka, Y., Mizushima, N., Ohsumi, Y. & Inagaki, F. (2004). The crystal structure of microtubule-associated protein light chain 3, a mammalian homologue of *Saccharomyces cerevisiae* Atg8. *Genes Cells*, **9**, 611–618.
23. Bavro, V. N., Sola, M., Bracher, A., Kneussel, M., Betz, H. & Weissenhorn, W. (2002). Crystal structure of the GABA(A)-receptor-associated protein, GABARAP. *EMBO Rep.* **3**, 183–189.
24. Shen, L. N., Liu, H., Dong, C., Xirodimas, D., Naismith, J. H. & Hay, R. T. (2005). Structural basis of NEDD8 ubiquitin discrimination by the deNEDylating enzyme NEDP1. *EMBO J.* **24**, 1341–1351.
25. Stubbs, M. T., Laber, B., Bode, W., Huber, R., Jerala, R., Lenarcic, B. & Turk, V. (1990). The refined 2.4 Å X-ray crystal structure of recombinant human stefin B in complex with the cysteine proteinase papain: a novel type of proteinase inhibitor interaction. *EMBO J.* **9**, 1939–1947.
26. Schneider, T. R. & Sheldrick, G. M. (2002). Substructure solution with SHELXD. *Acta Crystallog. sect. D*, **58**, 1772–1779.
27. Perrakis, A., Morris, R. & Lamzin, V. S. (1999). Automated protein model building combined with iterative structure refinement. *Nature Struct. Biol.* **6**, 458–463.
28. McRee, D. E. (1999). XtalView/Xfit–A versatile program for manipulating atomic coordinates and electron density. *J. Struct. Biol.* **125**, 156–165.
29. Murshudov, G. N., Vagin, A. A., Lebedev, A., Wilson, K. S. & Dodson, E. J. (1999). Efficient anisotropic refinement of macromolecular structures using FFT. *Acta Crystallog. sect. D*, **55**, 247–255.

Edited by K. Morikawa

(Received 13 September 2005; received in revised form 4 November 2005; accepted 6 November 2005)
Available online 28 November 2005

THE JOURNAL OF BIOLOGICAL CHEMISTRY VOL. 281, NO. 7, pp. 4035–4041, February 17, 2006

Excess Peroxisomes Are Degraded by Autophagic Machinery in Mammals*

Received for publication, November 15, 2005 Published, JBC Papers in Press, December 6, 2005, DOI 10.1074/jbc.M512283200

Jun-ichi Iwata[‡§1], Junji Ezaki[‡1], Masaaki Komatsu[‡§], Sadaki Yokota[¶], Takashi Ueno[‡], Isei Tanida[‡], Tomoki Chiba[§], Keiji Tanaka[§], and Eiki Kominami[‡2]

From the [‡]Department of Biochemistry, Juntendo University School of Medicine, Bunkyo-ku, Tokyo 113-8421, the [§]Department of Molecular Oncology, Tokyo Metropolitan Institute of Medical Science, Bunkyo-ku, Tokyo 113-8613, and the [¶]Biology Laboratory, Interdisciplinary Graduate School of Medicine and Engineering, University of Yamanashi, Tamaho-machi, Yamanashi 409-38, Japan

Peroxisomes are degraded by autophagic machinery termed "pexophagy" in yeast; however, whether this is essential for peroxisome degradation in mammals remains unknown. Here we have shown that *Atg7*, an essential gene for autophagy, plays a pivotal role in the degradation of excess peroxisomes in mammals. Following induction of peroxisomes by a 2-week treatment with phthalate esters in control and *Atg7*-deficient livers, peroxisomal degradation was monitored within 1 week after discontinuation of phthalate esters. Although most of the excess peroxisomes in the control liver were selectively degraded within 1 week, this rapid removal was exclusively impaired in the mutant liver. Furthermore, morphological analysis revealed that surplus peroxisomes, but not mutant hepatocytes, were surrounded by autophagosomes in the control. Our results indicated that the autophagic machinery is essential for the selective clearance of excess peroxisomes in mammals. This is the first direct evidence for the contribution of autophagic machinery in peroxisomal degradation in mammals.

Reorganization of organelles constitutively or suddenly occurs in eukaryotic cells as an adaptation to environmental changes accompanying the cell cycle, development, and differentiation (1). Such alterations are stringently regulated by biogenesis and/or degradation. In the last decade, much attention was paid to the study of organelle assembly, an interest linked with the translocation of proteins into the organelles (2). One focus of that work was peroxisomes. Peroxisomes are single membrane-bound organelles that contribute to an array of metabolic pathways and are specifically and markedly induced by a group of non-genotoxic carcinogens and endogenous steroids in rodents (3-6). Indeed, peroxisome proliferators increase the size, number, and enzymes involved in fatty acid metabolism: *e.g.* peroxisomal thiolase (PT),[3] peroxisomal bifunctional protein (BF), and fatty acid β-oxidation of peroxisomes (7, 8). However, the mechanistic basis of peroxisome turnover remains poorly understood (8, 9).

In yeast species, such as *Pichia pastoris, Hansenula polymorpha, Candida boidinii,* and *Saccharomyces cerevisiae*, proliferating peroxisomes are degenerated by an autophagy-related process named pexophagy during glucose or ethanol adaptation (10–14). Yeast genetics of pexophagy revealed that most autophagy-related (*Atg*) genes play indispensable roles in this selective degradation of peroxisomes as well as autophagy (8, 9, 13, 15, 16). In mammals, however, whether or not the autophagic machinery is involved in the degradation of excess peroxisomes biosynthesized in response to drug cues remains a mystery. In particular, there is no direct evidence for the degradation of disused peroxisomes by the autophagic machinery, and it is not clear whether such a degradation process, if any, is selective or non-selective. It has also been reported that selective degradation of mitochondria may occur via autophagy-related mechanism in yeast (17, 18). Therefore, selectivity in the organelle turnover via autophagy is an important issue.

Among the many *Atg* genes that regulate autophagy, *Atg7*, which encodes a ubiquitin-activating enzyme (E1)-like enzyme common to two ubiquitylation-like conjugations, the LC3 (*Atg8* in yeast) and Atg12 conjugation systems, is a critical gene for autophagosome formation in yeast and mammalian cells (19–26). It has been reported that in yeast, *Atg7/Apg7/Gsa7* is essential for pexophagy in addition to autophagy (19, 22, 24). During mammalian autophagy, LC3-I (a cytosolic form of LC3) is lipidated to LC3-II (its autophagosomal membrane-bound form) by Atg7 (an E1-like enzyme) and Atg3 (a ubiquitin carrier protein (E2)-like enzyme) (21, 27). Recently, we have established conditional knock-out-mice of Atg7 and have shown that Atg7 is indispensable for mammalian autophagy and that the autophagy deficiency in liver leads to marked accumulation of cytoplasmic proteins (20). In the normal liver, LC3 is continuously synthesized to form LC3-I, and LC3-I is subsequently conjugated with phosphatidylethanolamine to form LC3-II during autophagy. LC3-II is then recruited to autophagosomal membranes (21, 28), and the autophagosomal LC3-II is rapidly degraded after fusion of autophagosome with lysosome (29). This dynamic flow of LC3 is completely inhibited in Atg7-deficient liver and, as a consequence, more LC3-I accumulates in the mutant liver (20). Considering that deletion of yeast *Atg7/Gsa7* gene results in a defect of pexophagy in *P. pastoris* (24), the liver-specific *Atg7*-conditional knock-out mice will be an advantageous tool in investigating the degradation of peroxisomes in mammals.

In this study, we analyzed the clearance of surplus peroxisomes using the conditional-knock-out mice of *Atg7* (20). The results indicated that autophagy is essential for the degradation of accumulated peroxisomes in the mouse liver.

EXPERIMENTAL PROCEDURES

Reagents—Phthalate esters (diethylhexyl phthalate (DEHP)), corn oil, and leupeptin were purchased from Sigma.

* This work was supported by Grants-in-aid 15032263, 16790195, 15590254, 09680629, and 1270040 from the Ministry of Education, Culture, Sports, Science and Technology of Japan. The costs of publication of this article were defrayed in part by the payment of page charges. This article must therefore be hereby marked "*advertisement*" in accordance with 18 U.S.C. Section 1734 solely to indicate this fact.

[1] Both authors contributed equally to this work.

[2] To whom correspondence should be addressed: Dept. of Biochemistry, Juntendo University School of Medicine, 2-1-1 Hongo, Bunkyo-ku, Tokyo 113-8421, Japan. Tel.: 81-3-5802-1031; Fax: 81-3-5802-5889; E-mail: komilabo@med.juntendo.ac.jp.

[3] The abbreviations used are: PT, peroxisomal thiolase; BF, bifunctional protein; DEHP, diethylhexyl phthalate; MLP, mitochondrial/lysosomal/peroxisomal; Atg, autophagy-related; BiP, binding protein; pIpC, polyinosinic acid-polycytidylic acid.

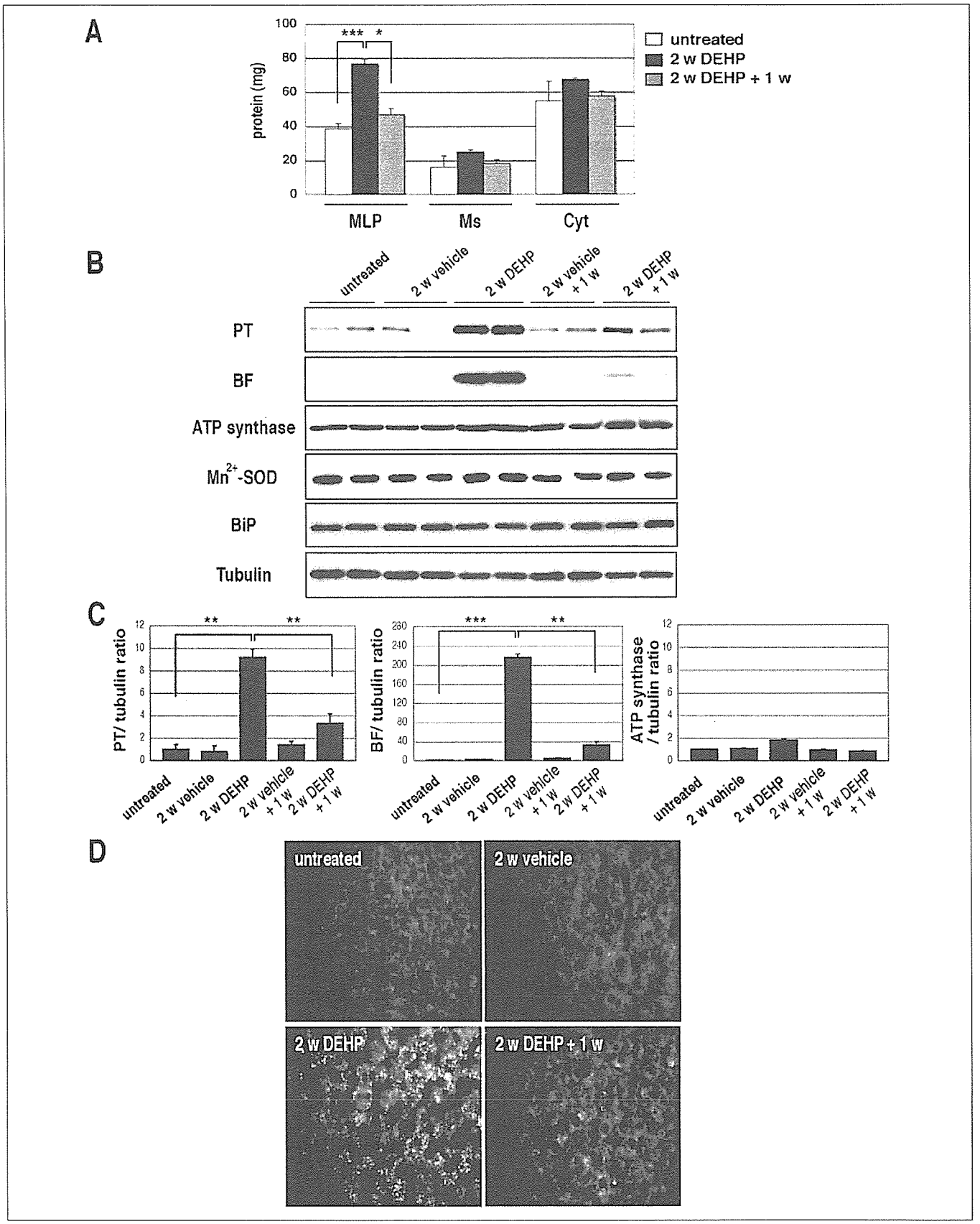

FIGURE 1. **The recovery process of excess peroxisomes induced by DEHP treatment.** *A*, wild-type mice were treated with DEHP for 2 weeks (*2 w DEHP*) and then chased for 1 week (*2 w DEHP + 1 w*). Untreated and treated mice were dissected, and liver homogenates were fractionated into MLP, microsomal (*Ms*), and cytosolic (*Cyt*) fractions. The protein amount in each fraction was measured. Data are mean ± S.D. values of five mice in each group; *, $p < 0.02$ and ***, $p < 0.001$. *B*, wild-type mice were treated as described in *A*. The vehicle

Animals and Treatment Regimen—C57B6J mice were used as wild-type mice. Male mice received DEHP (1,150 mg/kg/day) or vehicle (corn oil, 5 ml/kg/day) via sonde daily for 2 weeks, and the mice were subsequently fed on a normal diet for 1 week to investigate the changes in proliferated peroxisomes during the recovery process according to the protocol reported previously (7). For detection of autophagosomes by electron microscopy, mice were injected with leupeptin (2 mg/100 g of body weight) after administration of DEHP. All animals were sacrificed by deep anesthesia.

Deletion of Atg7 in Mouse Liver—Atg7 conditional knock-out mice and the heterozygotes were prepared as described previously (20). Briefly, creatine expression in the liver was induced by intraperitoneal injection of polyinosinic acid-polycytidylic acid (pIpC). pIpC was injected three times at a 48-h interval.

Preparation of the Fractions—Livers from $Atg7^{F/+}$:Mx1 and $Atg7^{F/F}$:Mx1 mice were treated with DEHP or corn oil for 2 weeks, and at 1 week after treatment, they were dissected. Subfractionation of the livers was accomplished by differential centrifugation according to the method of de Duve *et al.* (30). Briefly, 20% homogenates were prepared in 0.25 M sucrose, 10 mM HEPES-NaOH, pH 7.4 (homogenizing buffer). The homogenate of the liver was centrifuged at 650 × *g* for 5 min to remove nuclei and unbroken cells. The pellets were resuspended in the same volume of homogenizing buffer and were then recentrifuged. The supernatants from these two centrifugations were combined and used as postnuclear supernatant fractions. Postnuclear supernatant fractions were centrifuged at 10,000 × *g* for 20 min, and pellets were used as the mitochondrial/lysosomal/peroxisomal (MLP) fractions. The post-MLP supernatants were further centrifuged at 105,000 × *g* for 60 min to precipitate microsomal fractions in pellet form. All procedures were performed at 4 °C.

Immunoblot Analysis—Immunoblotting was performed as described previously (19). The antibody against Mn^{2+}-superoxide dismutase was kindly provided by Prof. Naoyuki Taniguchi (Osaka University, Japan). The antibodies for Atg7 (19), LC3 (20), BF (31), PT (32), and the β-subunit of ATP synthase (33) were prepared as described previously. The antibodies against tubulin and BiP were purchased from Chemicon International, Inc. (Temecula, CA) and Affinity BioReagents, Inc. (Golden, CO), respectively.

Histological Examination—Livers were dissected, fixed in 4% paraformaldehyde, frozen, embedded, and sectioned. For immunohistochemical analysis, the sections were blocked with 5% normal goat serum in phosphate-buffered saline containing 0.2% Triton X-100 and then incubated with anti-PT antibody and Alexa Fluor 488-labeled second antibody (Molecular Probes, Eugene, OR). Fluorescence images were obtained using a fluorescence microscope (Q550FV; Leica, Germany) equipped with cooled charge-coupled device camera (CTR MIC; Leica). Pictures were taken using Leica Qfluoro software (Leica).

Electron Microscopy—Livers were perfusion-fixed with the fixative through the portal vein for 10 min. The fixative consisted of 2% paraformaldehyde, 1% glutaraldehyde, and 0.1 M HEPES-KOH buffer (pH 7.4). To visualize peroxisomes, some liver slices were incubated in alkaline 3,3-diaminobendine medium consisting of 2 mg/ml 3,3-diaminobendine, 0.02% hydrogen peroxide, and 0.2 M glycine-NaOH buffer (pH 10.0) for 1 h at room temperature. Then they were postfixed with 1% reduced osmium tetroxide for 1 h. The other tissue slices were postfixed in 1% reduced osmium tetroxide with 3,3-diaminobendine reaction. All tissue slices were then dehydrated in graded series of ethanol and embedded in Epon. Thin sections were cut with a diamond knife using an ultramicrotome (Reichert, Vienna, Austria). Sections were contrasted with 40 mM lead citrate for 5 min and examined with a Hitachi H7500 electron microscope (Hitachi, Tokyo, Japan).

Quantitative Analysis of Peroxisomes—For each tissue slice, 20 digital electron micrographs were acquired at ×5,000 magnification, enlarged 2.7-fold, and printed by a laser printer. Using the printed figure, we measured the area of peroxisomes and that of the cytoplasmic area of hepatocytes using a SigmaScan scientific measurement system equipped with a computer (Jandel Scientific, San Rafael, CA). The relative total area of peroxisomes was calculated using the following formula: (number of peroxisomes in the average area of peroxisomes/cytoplasmic area) and expressed in $\mu m^2/100\ \mu m^2$ of cytoplasmic area.

Statistical Analysis—The statistical significance of differences between experimental and control groups was determined by the two-tailed Student's *t* test. A *p* value of <0.05 was considered statistically significant.

RESULTS

Selective Degradation of Excess Peroxisomes—Phthalate ester (DEHP) and its active metabolite mono-ethylhexyl phthalate can cause marked increases in both the size and the number of peroxisomes and induce peroxisomal enzymes in the liver (7). Utilizing these phenomena, we first investigated the specific proliferation of peroxisomes and the rapid recovery after removal of the drugs in mice. Wild-type mice were treated with DEHP for 2 weeks and then chased for 1 week as described under "Experimental Procedures." The mice were dissected at each period, and the liver cell lysates were fractionated into MLP, microsomal, and cytosolic fractions. DEHP administration for 2 weeks was associated with about 2-fold increase in the amount of total protein in MLP, but not in microsomal or cytosolic fractions, as compared with untreated mice, and the amount almost returned to the basal level at 1 week after discontinuation of DEHP (Fig. 1*A*). These changes were not observed in mice treated with the vehicle (data not shown). Quantitative densitometric analysis of immunoblotting data revealed that PT and BF, marker proteins of peroxisomes, increased significantly after administration of DEHP but not the vehicle, and both diminished significantly to basal levels at 1 week after DEHP discontinuation (Fig. 1, *B* and *C*). In comparison, the levels of mitochondrial proteins, the β-subunit of ATP synthase and manganese superoxide dismutase, and the endoplasmic reticulum marker, BiP, remained unchanged during the same manipulations (Fig. 1*B*). Immunofluorescence analysis using anti-PT antibody revealed that a 2-week administration of DEHP, but not the vehicle, resulted in the appearance of numerous dots representing peroxisomes, and most of these dots disappeared at 1 week after discontinuation of DEHP (Fig. 1*D*). Considered together, these results indicate that DEHP-induced peroxisomes are selectively degraded following removal of the peroxisome proliferator.

Impairment of Degradation of Proliferated Peroxisomes in Autophagy-deficient Liver—Next, to examine the effects of autophagy deficiency on peroxisome degradation, we took advantage of the conditional knock-out mice, $Atg7^{F/F}$:Mx1 (mutant mice), and their littermates, $Atg7^{F/+}$:Mx1 mice (control mice), the systems of which

control mice were treated with corn oil for 2 weeks (*2 w vehicle*). Untreated and treated mice were sacrificed, and the livers were dissected out and homogenized, and then the postnuclear supernatant fractions were subjected to immunoblotting with anti-PT, BF, β-subunit ATP synthase, Mn^{2+}-superoxide dismutase (*SOD*), BiP, and tubulin antibodies. Tubulin was used as a control. Data shown are representative of three separate experiments. *C*, quantitative densitometry of immunoblotting data in *B* was performed, and the ratios between each of PT, BF, and ATP synthase and tubulin were plotted; **, $p < 0.01$, ***, $p < 0.001$. *D*, wild-type mice were treated with DEHP as described in *A*, and the frozen sections of livers were stained with anti-PT antibody to detect peroxisomes. Magnification, ×400.

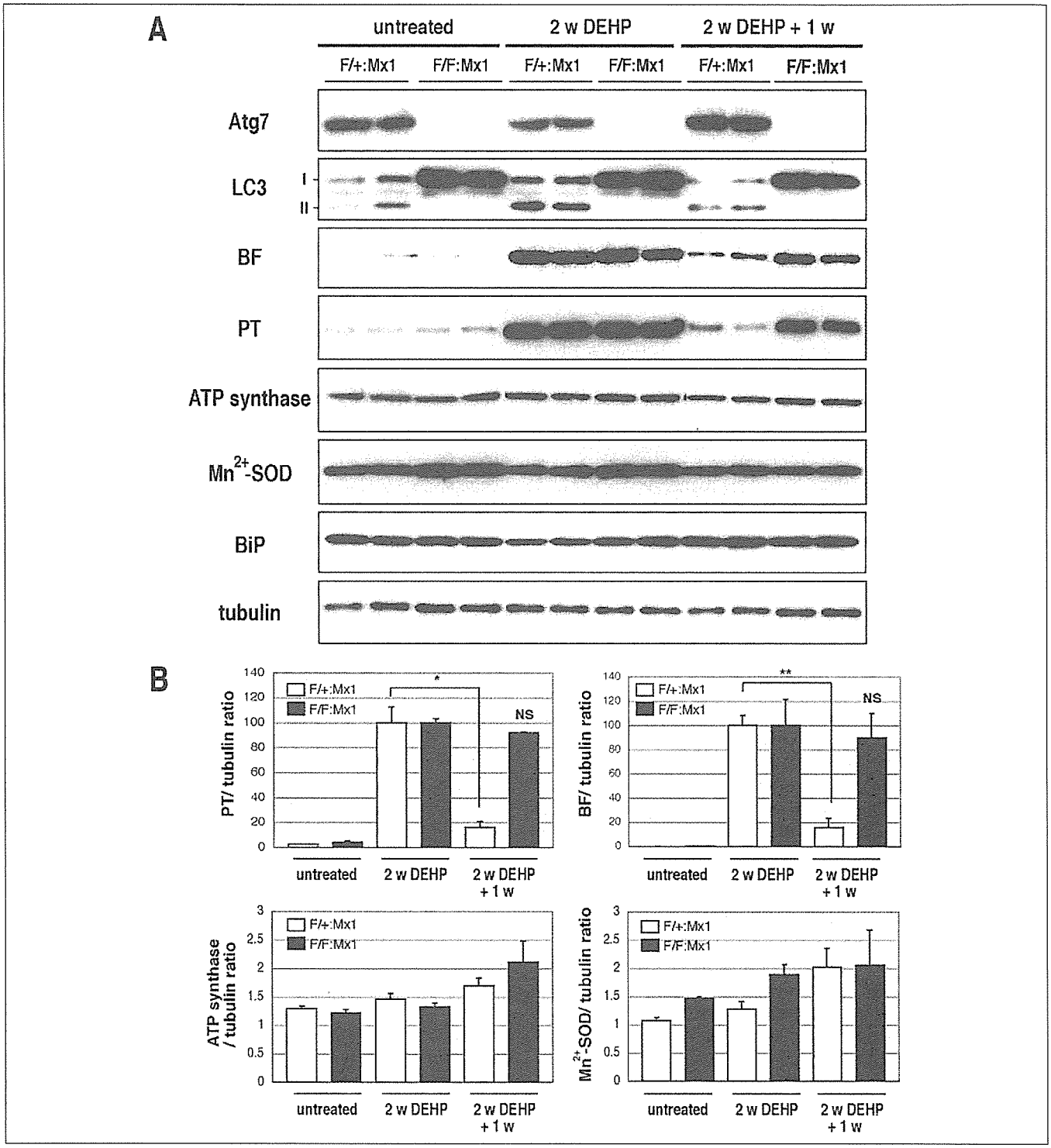

FIGURE 2. **The recovery process of excess peroxisomes is impaired in *Atg7*-deficient liver.** *A*, $Atg7^{F/+}$:Mx1 (*F/+:Mx1*) and $Atg7^{F/F}$:Mx1 (*F/F:Mx1*) mice were treated with DEHP for 2 weeks (*2 w DEHP*) and then chased for 1 week (*2 w DEHP + 1 w*). Both genotype mice were sacrificed at each time point. The liver was dissected out and homogenized, and then the postnuclear supernatant fractions were subjected to immunoblotting using anti-Atg7, LC3, BF, PT, β-subunit ATP synthase, Mn^{2+}-superoxide dismutase (*SOD*), BiP, and tubulin antibodies. Tubulin was used as control. Data shown are representative of three separate experiments. *B*, quantitative densitometry of Western blotting shown in *A* was performed, and PT/tubulin, BF/tubulin, β-subunit ATP synthase/tubulin, and Mn^{2+}-superoxide dismutase/tubulin ratios were plotted; *, $p < 0.02$, **, $p < 0.01$, *NS*; not significant.

were recently established by our group (20). Autophagy is impaired following pIpC injection in $Atg7^{F/F}$:Mx1 mouse livers. Indeed, we verified that Atg7 protein deletion in $Atg7^{F/F}$:Mx1 but not $Atg7^{F/+}$:Mx1 livers was pIpC injection-dependent (Fig. 2*A*). Furthermore, we also tested the loss of Atg7 activity by investigating the lack of LC3-II (a membrane-bound form of LC3) and accumulation of LC3-I (a cytosolic form of LC3) in the liver. It is generally accepted that LC3-II is a marker protein of autophagosomal membranes (21). Although both forms were detected in the control liver, only LC3-I accumulated in the mutant liver (Fig. 2*A*), indicating impairment of autophagy in mutant $Atg7^{F/F}$:Mx1

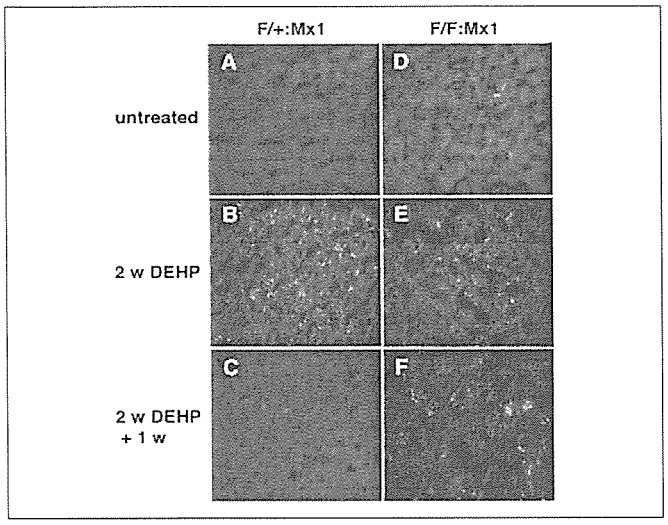

FIGURE 3. **Accumulation of excess peroxisomes in *Atg7*-deficient liver.** Immunofluorescent detection of peroxisomes with anti-PT antibody in the $Atg7^{F/+}$:Mx1 (*A–C, F/+:Mx1*) and $Atg7^{F/F}$:Mx1 (*D–F, F/F:Mx1*) liver is shown. $Atg7^{F/+}$:Mx1 and $Atg7^{F/F}$:Mx1 mice were treated with DEHP for 2 weeks (*B* and *E, 2 w DEHP*) and then chased for 1 week (*C* and *F, 2 w DEHP + 1 w*). Untreated (*A* and *D*) and treated mice were sacrificed, and the livers were isolated. The frozen sections of livers were immunostained with anti-PT antibody. Magnification, ×400.

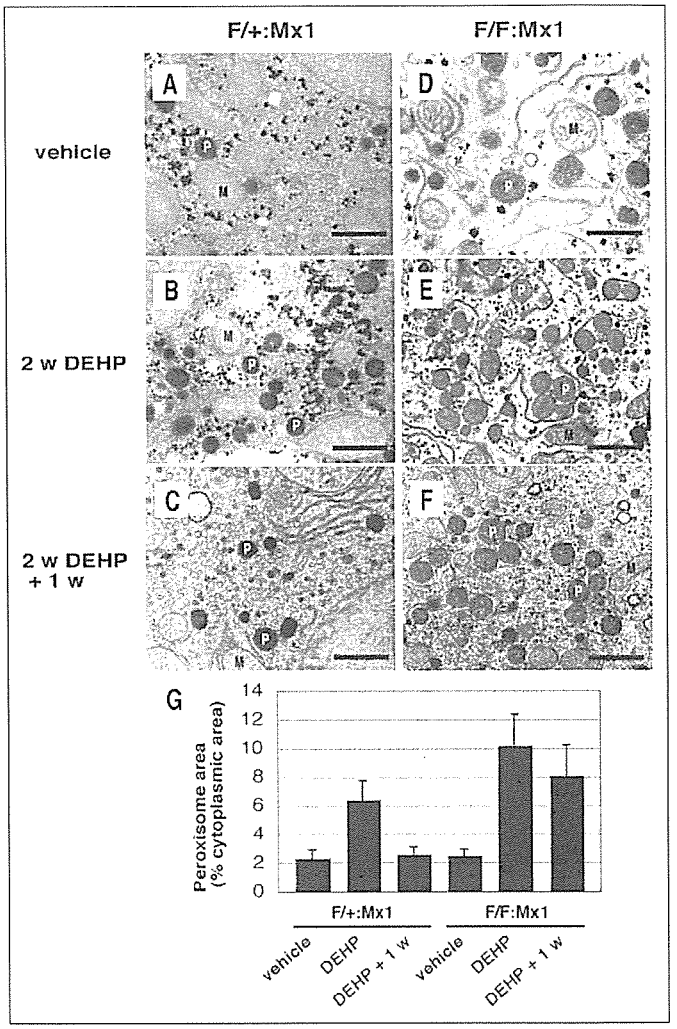

FIGURE 4. **Electron microscopic evaluation of livers of *Atg7*-deficient mice treated with DEHP.** *A–F*, electron micrographs of the liver of representative $Atg7^{F/+}$:Mx1 mice (*F/+:Mx1*) and $Atg7^{F/F}$:Mx1 (*F/F:Mx1*) mice treated with DEHP for 2 weeks (*B* and *E, 2 w DEHP*) and then fed on normal diet for 1 week (*C* and *F, 2 w DEHP + 1 w*). The vehicle control mice of each genotype were treated with corn oil for 2 weeks (*A* and *D*). The hepatocytes of both genotypes contained a high number of peroxisomes (*P*) after DEHP treatment (*B* and *E*). Note that induced peroxisomes were retained at 1 week after discontinuation of DEHP in $Atg7^{F/F}$:Mx1 hepatocytes, in contrast to the decreased number in $Atg7^{F/+}$:Mx1 hepatocytes (*C* and *F*). *Bars*, 1 μm. The total area of peroxisomes relative to the cytoplasmic area was determined in each genotype ($n = 10$). *M*, mitochondria; *G*, morphometric analysis of peroxisomes in $Atg7^{F/+}$:Mx1 and $Atg7^{F/F}$:Mx1 mice.

mouse liver (20). In the control livers, although LC3-II were induced by the proliferated peroxisomes (Fig. 2*A*, indicated by *2 w DEHP*), it was decreased almost to the basal levels at 1 week after withdrawal of DEHP (Fig. 2*A*), suggesting that autophagy was induced to remove surplus peroxisomes. After a 2-week treatment with DEHP, the livers were dissected, and total proteins in the lysates of mutant and control livers were separated by SDS-PAGE and subjected to immunoblot analyses. Similar to the results obtained with wild-type mice (Fig. 1), BF and PT increased profoundly after the treatment as compared with mice prior to DEHP administration and then decreased almost to the basal levels at 1 week after discontinuation in $Atg7^{F/+}$:Mx1 livers (Fig. 2, *A* and *B*). Although this increase was also detected in mutant $Atg7^{F/F}$:Mx1 livers, the increased PT and BT proteins did not return to the basal levels following the discontinuation of DEHP (Fig. 2, *A* and *B*). In contrast to peroxisomal proteins, the levels of mitochondrial (β-subunit of ATP synthase and Mn^{2+}-superoxide dismutase) and endoplasmic reticulum (BiP) markers did not change under these conditions (Fig. 2, *A* and *B*). These results indicate selective impairment of degradation of excess peroxisomal proteins in autophagy-deficient $Atg7^{F/F}$:Mx1 liver.

We further confirmed the impairment of peroxisome degradation in autophagy-deficient liver by immunofluorescence analysis using anti-PT antibody (Fig. 3). The PT-positive dots representing peroxisomes were markedly increased following a 2-week DEHP treatment in both genotype livers, as compared with untreated mice (Fig. 3, *A* and *D versus B* and *E*). Although the dots almost disappeared to the basal levels at 7 days after discontinuation of DEHP in the control (Fig. 3*C*), most of the peroxisome dots remained visible in mutant liver after the same intervention (Fig. 3*F*). The data are in agreement with the biochemical results shown in Fig. 2. Based on these results, we concluded that autophagy is essential for selective degradation of excess peroxisomes.

Engulfment of Excess Peroxisomes by Autophagosomal Membranes in Control Hepatocytes—Finally, we used electron microscopy to explore the level of the peroxisomes in $Atg7^{F/F}$:Mx1 and $Atg7^{F/+}$:Mx1 livers (Fig. 4). Consistent with the results of immunofluorescent analysis, numerous peroxisomes were detected following a 2-week DEHP treatment in both wild and mutant hepatocytes (Fig. 4, *B* and *E*), and most of these structures disappeared after 1 week of discontinuation of DEHP in the control, but not mutant, hepatocytes (Fig. 4, *C* and *F*). The relative total area of peroxisomes was determined, and the mean values are shown in Fig. 4*G*. Although the relative total area of peroxisomes increased in both groups after a 2-week DEHP administration, the area decreased to the basal level in control hepatocytes, but not in mutant hepatocytes, at 1 week after DEHP withdrawal from the diet (Fig. 2*G*).

After discontinuation of DEHP, we detected only a few autophagosome-like structures in control hepatocytes, probably due to the rapid turnover of autophagosomes by lysosome (Fig. 4*C*). Considering the selective degradation of peroxisomal marker proteins, PT and BF (Fig. 2), autophagosomes that selectively enwrap peroxisomes could be observed by electron microscopic analysis when lysosomal proteolysis is inhibited. Therefore, we examined whether proliferated peroxisomes enclosed by autophagosomal membranes can be detected under the condition of inhibited autophagic proteolysis. Injection of leupeptin, a

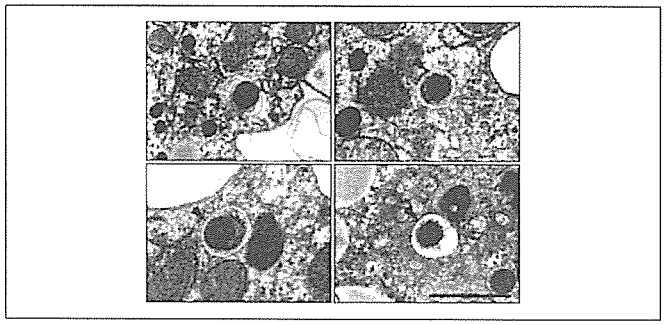

FIGURE 5. **Excess peroxisomes are surrounded by autophagosome.** $Atg7^{F/+}$:Mx1 mice were treated with DEHP for 2 weeks and then injected with leupeptin as described under "Experimental Procedures." The mice were sacrificed, and the livers were dissected out and processed for electron microscopic examination. These images show representative autophagosomes surrounding peroxisomes. Four typical electron micrographs are represented. *Arrowheads* indicate the engulfment of peroxisome(s) by isolated membranes. *Bars*, 1 μm.

lysosomal cysteine proteinase inhibitor, into a 2-week DEHP-treated control $Atg7^{F/+}$:Mx1 mouse resulted in marked accumulation of autophagosomes, and some peroxisomes were surrounded by a double-membrane structure, autophagosome, in control hepatocytes (Fig. 5). No autophagosome was identified in hepatocytes of $Atg7^{F/F}$:Mx1 mice (data not shown). These lines of evidence indicated that the autophagic machinery mediated is essential for selective clearance of excess peroxisomes, as it is so for starvation-induced autophagy in the mouse liver.

DISCUSSION

Most cellular components, if not all, are regulated quantitatively to maintain cell homeostasis. For this regulation, there are growing lines of evidence for the importance of the balance between biosynthesis and degradation. Peroxisomes, a typical cellular component, are dynamic organelles induced and degraded in response to extracellular cues (8). However, little is known about the mechanism for peroxisome degradation in mammals. There are two major concepts for degradation of peroxisomes, *i.e.* autophagic machinery and autolysis (34, 35). By the analysis of autophagy-deficient livers, we showed the first direct evidence that peroxisomal breakdown is mainly, if not entirely, dependent on autophagic machinery. Based on quantitative densitometry with two peroxisome marker enzymes (Fig. 2, PT and BF) as well as morphometry of the electron micrographs (Fig. 4), ~70–80% of peroxisomes induced by DEHP were degraded via autophagy during 1 week after discontinuation of the drug administration.

Considering peroxisome degradation by autophagic machinery in mammals, it is important to know whether the process occurs via micropexophagy or macropexophagy. In methylotrophic yeast species, it is well established that the autophagy-related process, termed pexophagy, induces a rapid and selective degradation of excess peroxisomes (13). In *P. pastoris* cells, following a shift from methanol to ethanol or glucose, unnecessary peroxisomes are degraded by macropexophagy and micropexophagy, respectively (9). Macropexophagy is the degradation pathway in which autophagosomes selectively surround excess peroxisomes. On the other hand, in micropexophagy, the excess peroxisomes are not degraded through autophagosome formation. The initial step in micropexophagy is invagination and septation of a vacuole followed by engulfment of the peroxisomes by the vacuole. In the final stage, the edges of the vacuole fuse with each other followed by vacuolar degradation of the peroxisomal membrane and its contents. Because *ATG7* is essential for both macropexophagy and micropexophagy in *P. pastoris* cells, it is plausible that excess peroxisomes in mammalian cells are also degraded by both macroautophagy and micropexophagy. Our data using electron microscopy revealed that autophagosomes preferentially surrounded excess peroxisomes in control hepatocytes (Fig. 5), suggesting that DEHP-induced peroxisomes are degraded mainly through the process of macropexophagy. Thus, we could show the selective role of autophagic machinery in the clearance of surplus peroxisomes after induction of peroxisomes by phthalate esters.

Recent studies provided evidence for the involvement of the autophagic machinery in selective sequestration of proteins in the cell. For example, the precursor form of aminopeptidase I (prApe1) is a selective cargo molecule of autophagy in yeast (36), and cytosolic acetaldehyde dehydrogenase (Ald6p) is preferentially transported to vacuoles via autophagosomes in yeast (37). Consistently, the autophagic machinery could also selectively eliminate pathogenic group A *Streptococci* invading the cells (38). These reports strongly suggest that autophagosomes sequester the cytosolic protein(s) and invading pathogens in a highly selective manner. We recently reported that *Atg7*-deficient hepatocytes exhibit impaired constitutive autophagy responsible for selective degradation of ubiquitinated proteins (20). Our previous findings together with the present results suggest that the autophagic process eliminates abnormal and/or excess proteins and organelles including peroxisomes in a selective manner even under normal conditions. How the autophagy machinery recognizes these organelles to degrade them awaits further investigation.

Acknowledgment—We thank Tsuguka Kouno for technical assistance.

REFERENCES

1. Lazarow, P. B., and Fujiki, Y. (1985) *Annu. Rev. Cell Biol.* **1,** 489–530
2. Heiland, I., and Erdmann, R. (2005) *FEBS J.* **272,** 2362–2372
3. Reddy, J. K., Azarnoff, D. L., Hignite, C. E. (1980) *Nature* **283,** 397–398
4. Reddy, J. K., Lalwani, N. D. (1983) *CRC Crit. Rev. Toxicol.* **12,** 1–58
5. Nicholls-Grzemski, F. A., Calder, I. C., and Priestly, B. G. (1992) *Biochem. Pharmacol.* **7,** 1395–1396
6. Vanden Henvel, J. P. (1999) *Toxicol. Sci.* **47,** 1–8
7. Yokota, S. (1993) *Eur. J. Cell Biol.* **61,** 67–80
8. Subramani, S. (1998) *Physiol. Rev.* **78,** 171–188
9. Farre, J. C., and Subramani, S. (2004) *Trends Cell Biol.* **14,** 515–523
10. Kim, J., Kamada, Y., Stromhaug, P. E., Guan, J., Hefner-Gravink, A., Baba, M., Scott, S. V., Ohsumi, Y., Dunn, W. A., Jr., and Klionsky, D. J (2001) *J. Cell Biol.* **153,** 381–396
11. Stromhaug, P. E., Bevan, A., and Dunn, W. A., Jr. (2001) *J. Biol. Chem.* **276,** 42422–42435
12. Bellu, A. R., Komori, M., Klei, I. J., Kiel, J. A., and Veenhuis, M. (2001) *J. Biol. Chem.* **276,** 44570–44574
13. Bellu, A. R., and Kiel, J. A. (2003) *Microsc. Res. Tech.* **61,** 161–170
14. Ano, Y., Hattori, T., Oku, M., Mukaiyama, H., Baba, M., Ohsumi, Y., Kato, N., and Sakai, Y. (2005) *Mol. Biol. Cell* **16,** 446–457
15. Klionsky, D. J., and Ohsumi, Y. (1999) *Annu. Rev. Cell Dev. Biol.* **15,** 1–32
16. Kim, J., and Klionsky, D. J. (2000) *Annu. Rev. Biochem.* **69,** 303–342
17. Kissova, I., Deffieu, M., Manon, S., and Camougrand, N. (2004) *J. Biol. Chem.* **279,** 39068–39074
18. Lemasters, J. J. (2005) *Rejuvenation Res.* **8,** 3–5
19. Tanida, I., Mizushima, N., Kiyooka, M., Ohsumi, M., Ueno, T., Ohsumi, Y., and Kominami, E. (1999) *Mol. Biol. Cell* **10,** 1367–1379
20. Komatsu, M., Waguri, S., Ueno, T., Iwata, J., Murata, S., Tanida, I., Ezaki, J., Mizushima, N., Ohsumi, Y., Uchiyama, Y., Kominami, E., Tanaka, K., and Chiba, T. (2005) *J. Cell Biol.* **169,** 425–434
21. Kabeya, Y., Mizushima, N., Ueno, T., Yamamoto, A., Kirisako, T., Noda, T., Kominami, E., Ohsumi, Y., and Yoshimori, T. (2000) *EMBO J.* **19,** 5720–5728
22. Mizushima, N., Noda, T., Yoshimori, T., Tanaka, Y., Ishii, T., George, M. D., Klionsky, D. J., Ohsumi, M., and Ohsumi, Y. (1998) *Nature* **395,** 395–398
23. Ichimura, Y., Kirisako, T., Takao, T., Satomi, Y., Shimonishi, Y., Ishihara, N., Mizushima, N., Tanida, I., Kominami, E., Ohsumi, M., Noda, T., and Ohsumi, Y. (2000) *Nature* **408,** 488–492
24. Yuan, W., Stromhaug, P. E., and Dunn, W. A., Jr. (1999) *Mol. Biol. Cell* **10,** 1353–1366
25. Tanida, I., Tanida-Miyake, E., Ueno, T., and Kominami, E. (2001) *J. Biol. Chem.* **276,** 1701–1706

26. Tanida, I., Tanida-Miyake, E., Nishitani, T., Komatsu, M., Yamazaki, H., Ueno, T., and Kominami, E. (2002) *Biochem. Biophys. Res. Commun.* **292,** 256–262
27. Tanida, I., Tanida-Miyake, E., Komatsu, M., Ueno, T., and Kominami, E. (2002) *J. Biol. Chem.* **277,** 13739–13744
28. Asanuma, K., Tanida, I., Shirato, I., Ueno, T., Takahara, H., Nishitani, T., Kominami, E., and Tomino, Y. (2003) *FASEB J.* **17,** 1165–1167
29. Tanida, I., Minematsu-Ikeguchi, N., Ueno, T., and Kominami, E. (2005) *Autophagy* **1,** 84–91
30. de Duve, C., Pressman, B. C., Gianetto, R., Wattiaux, R., and Appelmans, F. (1955) *Biochem. J.* **60,** 604–617
31. Usuda, N., Yokota, S., Ichikawa, R., Hashimoto, T., and Nagata, T. (1991) *J. Histochem. Cytochem.* **39,** 95–102
32. Tsukamoto, T., Yokota, S., and Fujiki, Y. (1990) *J. Cell Biol.* **110,** 651–660
33. Ezaki, J., Wolfe, L. S., Higuti, T., Ishidoh, K., and Kominami, E. (1995) *J. Neurochem.* **64,** 733–741
34. Yokota, S., Oda, T., and Fahimi, H. D. (2001)) *J. Histochem. Cytochem.* **49,** 613–621
35. Yokota, S. (2003) *Microsc. Res. Tech.* **61,** 151–160
36. Shintani, T., and Klionsky, D. J. (2004) *J. Biol. Chem.* **279,** 29889–29894
37. Onodera, J., and Ohsumi, Y. (2004) *J. Biol. Chem.* **279,** 16071–16076
38. Nakagawa, I., Amano, A., Mizushima, N., Yamamoto, A., Yamaguchi, H., Kamimoto, T., Nara, A., Funao, J., Nakata, M., Tsuda, K., Hamada, S., and Yoshimori, T. (2004) *Science* **306,** 1037–1040

THE JOURNAL OF BIOLOGICAL CHEMISTRY
Vol. 280, No. 22, Issue of June 3, pp. 21515–21521, 2005
Printed in U.S.A.

Unsaturated Fatty Acids Induce Cytotoxic Aggregate Formation of Amyotrophic Lateral Sclerosis-linked Superoxide Dismutase 1 Mutants*

Received for publication, February 28, 2005
Published, JBC Papers in Press, March 29, 2005, DOI 10.1074/jbc.M502230200

Yeon-Jeong Kim‡, Reiko Nakatomi§, Takumi Akagi§, Tsutomu Hashikawa§, and Ryosuke Takahashi‡¶‖

From the Laboratories for ‡Motor System Neurodegeneration and §Neural Architecture, RIKEN Brain Science Institute, Saitama 351-0198, Japan and ¶Department of Neurology, Kyoto University Graduate School of Medicine, Kyoto 606-8507, Japan

Formation of misfolded protein aggregates is a remarkable hallmark of various neurodegenerative diseases including Alzheimer disease, Parkinson disease, Huntington disease, prion encephalopathies, and amyotrophic lateral sclerosis (ALS). Superoxide dismutase 1 (SOD1) immunoreactive inclusions have been found in the spinal cord of ALS animal models and patients, implicating the close involvement of SOD1 aggregates in ALS pathogenesis. Here we examined the molecular mechanism of aggregate formation of ALS-related SOD1 mutants *in vitro*. We found that long-chain unsaturated fatty acids (FAs) promoted aggregate formation of SOD1 mutants in both dose- and time-dependent manners. Metal-deficient SOD1s, wild-type, and mutants were highly oligomerized compared with holo-SOD1s by incubation in the presence of unsaturated FAs. Oligomerization of SOD1 is closely associated with its structural instability. Heat-treated holo-SOD1 mutants were readily oligomerized by the addition of unsaturated FAs, whereas wild-type SOD1 was not. The monounsaturated FA, oleic acid, directly bound to SOD1 and was characterized by a solid-phase FA binding assay using oleate-Sepharose. The FA binding characteristics were closely correlated with the oligomerization propensity of SOD1 proteins, which indicates that FA binding may change SOD1 conformation in a way that favors the formation of aggregates. High molecular mass aggregates of SOD1 induced by FAs have a granular morphology and show significant cytotoxicity. These findings suggest that SOD1 mutants gain FA binding abilities based on their structural instability and form cytotoxic granular aggregates.

Amyotrophic lateral sclerosis (ALS)[1] is a progressive and fatal neurodegenerative disorder that mainly affects motor neurons in the brain stem and spinal cord. Approximately 10% of ALS patients are familial cases, with autosomal dominant inheritance. More than 90 different mutations in the gene coding for superoxide dismutase 1 (SOD1) have been identified in about 20% of familial ALS (FALS) families (1, 2). Although the molecular mechanisms of selective motor neuron degeneration by SOD1 mutants in FALS remain largely unknown, common pathological features of conformational diseases, as evidenced by SOD1 immunoreactive inclusions, are found in the spinal cord of ALS patients and in the SOD1 mutant FALS mouse model (3–8). The characteristics of FALS resemble those of many other neurodegenerative diseases in which a causative protein undergoes a conformational rearrangement, which endows it with a tendency to aggregate and form deposits within affected tissues.

SOD1 is a 32-kDa homodimeric enzyme that decreases the intracellular concentration of superoxide radicals by catalyzing their dismutation to O_2 and H_2O_2. ALS-linked mutations of SOD1 are distributed throughout the primary and tertiary structures, and most mutations appear unrelated to the dismutase activity. Many biochemical and biophysical studies have reported that SOD1 mutants are structurally unstable compared with wild-type forms (10–13). These observations suggest that the mutations primarily affect the structural stability of SOD1 rather than the enzyme activity.

The half-life of SOD1 mutants is shorter than that of wild-type forms in cultured cells (14). SOD1 mutants form a complex with Hsp70 and CHIP, which promotes degradation of SOD1 through the ubiquitin-proteasome system (15). Hsp70 directly binds metal-deficient wild-type SOD1 as well as SOD1 mutants, suggesting that destabilized SOD1 is targeted by the molecular chaperone system (15, 16). These observations imply that structural stability of SOD1 may also be strongly involved in refolding by the chaperone or in degradation of SOD1 by the ubiquitin-proteasome system. On the other hand, aggregates of mutant SOD1 are observed to have aggresome-like morphology when cells are treated with a proteasome inhibitor (14). This aggresome-like morphology resembles pathological inclusions of neurodegenerative diseases in affected tissues. These findings suggest that in disease states, misfolded proteins overwhelm the protein handling systems, including chaperones and proteasomes. Therefore, the formation of cellular inclusions may be required for other factors to act as modulators to promote protein aggregates. In fact, lipid molecules, including unsaturated fatty acids (FAs), phosphatidylserine, and phosphatidylinositol, promote amyloidogenesis of amyloid β-peptides, tau (17), and α-synuclein (18, 19) *in vitro*. These molecules are biologically significant as mediators for signal-

* This work was supported by research grants from RIKEN Brain Science Institute and a grant-in-aid from the Ministry of Education, Culture, Sports, and Technology of Japan. The costs of publication of this article were defrayed in part by the payment of page charges. This article must therefore be hereby marked "*advertisement*" in accordance with 18 U.S.C. Section 1734 solely to indicate this fact.

‖ To whom correspondence should be addressed: Dept. of Neurology, Kyoto University Graduate School of Medicine, 54 Kawahara-cho, Shogoin, Sakyo-ku, Kyoto 606-8507, Japan. Tel.: 81-75-751-3770; Fax: 81-75-761-9780; E-mail: ryosuket@kuhp.kyoto-u.ac.jp.

[1] The abbreviations used are: ALS, amyotrophic lateral sclerosis; FALS, familial amyotrophic lateral sclerosis; SOD1, superoxide dismutase 1; FA, fatty acid; AA, arachidonic acid; MTS, 3-(4,5-dimethylthiazol-2-yl)-5-(3-carboxymethoxyphenyl)-2-(4-sulfophenyl)-2*H*-tetrazolium.

ing and inflammation during disease progression of neurodegeneration.

Here we investigated *in vitro* SOD1 aggregation affected by FAs to create an aggregation model system for FALS. We demonstrated that unsaturated FAs promote self-assembly and cytotoxic aggregate formation of SOD1. Aggregation by FAs is strongly correlated with structural instability and FA binding activity of SOD1, which may have significant implications in FALS.

EXPERIMENTAL PROCEDURES

Expression, Purification, and Characterization of Recombinant SOD1 Proteins—pcDNA3-SOD1 (20) was digested with EcoRV and XhoI and subcloned into blunted NcoI and XhoI sites of pET-15(b) (Novagen) to construct the expression plasmid. Expression of recombinant SOD1 proteins was induced in BL21(DE3)pLysS by adding 1 mM isopropyl 1-thio-β-D-galactopyranoside, 0.1 mM $CuCl_2$, and 0.1 mM $ZnCl_2$ until cells were grown to 0.6 absorbance unit at 600 nm, and then bacterial cells were further cultured at 23 °C for 6 h. Cells were pelleted and resuspended in TNE buffer (50 mM Tris-HCl, pH 8.0, 150 mM NaCl, and 0.1 mM EDTA) supplemented with protease inhibitor mixture (Roche Applied Science). Cells were then disrupted by sonication. Insoluble materials were removed by centrifugation at 10,000 × *g* for 30 min. Supernatant was collected for further purification. Purification was performed according to Hayward *et al.* (11), with minor modifications. Briefly, ammonium sulfate powder was added to the supernatant to 65% saturation with gentle stirring on ice. The supernatant, after centrifugation at 10,000 × *g* for 30 min, was directly loaded for phenyl-Sepharose (Amersham Biosciences) column chromatography. The column was thoroughly washed with TNE buffer containing 2 M ammonium sulfate. Proteins were eluted using a linearly decreasing salt gradient. SOD1 activity measurement using a xanthine/xanthine oxidase-based method (21) identified fractions containing SOD1. Activity fractions were desalted by ultrafiltration using a centricon filter (Millipore). SOD1 was re-metallated as described previously (22). The proteins were then loaded onto a Q-Sepharose (Amersham Biosciences) anion exchange column and eluted using a linearly increasing salt gradient toward a buffer containing 200 mM NaCl and 10 mM Tris-HCl, pH 8.0. Fractions containing SOD1 were pooled and concentrated. Homogeneity of SOD1 was >95%, as verified by SDS-PAGE with Coomassie Brilliant Blue staining. Specific activity of the purified enzymes was assayed and calculated by bovine SOD1 (Cayman) or human SOD1 purified from erythrocytes (Sigma-Aldrich) as standards. Fully metallated SOD1 was delipidated using hydroxyalkoxypropyl dextran type III (Sigma-Aldrich) as described previously (19) before de-metallation. Metal-deficient apo-enzymes were prepared as described previously (23), and loss of enzyme activity was confirmed after de-metallation. The metal content of purified enzymes was estimated as described previously (22).

Oligomerization of SOD1—A stock solution of 25 mM FAs was prepared in 0.01 M NaOH containing 25 μM butylated hydroxytoluene. SOD1 proteins were filtered through Microcon YM-100 (100-kDa cutoff) filters (Millipore) to remove high molecular mass SOD1 before oligomerization. FAs were added directly to preincubated SOD1 at 37 °C in 50 mM phosphate buffer, pH 7.2, containing 150 mM NaCl and 0.1 mM EDTA and further incubated at the same temperature.

SDS-PAGE and Western Blotting—For detection of SOD1 oligomers, SDS-PAGE was performed under non-reducing conditions using 12.5% polyacrylamide gels. After oligomerization of SOD1, protein samples were prepared in SDS-PAGE loading buffer (62.5 mM Tris-HCl, pH 6.8, 1% SDS, 5% glycerol, and 0.007% bromphenol blue) in the absence of β-mercaptoethanol and then boiled at 95 °C for 3 min before loading. Western blotting was performed as described previously (24). Briefly, proteins were transferred to Hybond ECL nitrocellulose membranes (Amersham Biosciences), followed by UV cross-linking, boiling membranes in 2% SDS and 50 mM Tris, pH 7.6, for 10 min, and extensive washing in Tris-buffered saline. For detection of SOD1, rabbit anti-SOD1 antibody (Stressgen) was used.

Glycerol Density Gradient Centrifugation and Densitometric Analysis—A glycerol linear gradient of 10–40% was prepared in a centrifuge tube. Formation of the SOD1 oligomer was performed as described above. Approximately 200 μl of incubated SOD1 was layered onto a glycerol cushion and separated by centrifugation with a SW41Ti rotor (Beckman) at 35,000 rpm for 15 h. In a parallel experiment, protein standards (Amersham Biosciences) were separated simultaneously in order to calibrate fractions. Fractions were subjected to SDS-PAGE under non-reducing conditions, and then Western blotting was performed. Western blot images were analyzed using image analysis software (Scion Image Beta 4.02; Scion Corp.).

Solid-phase Oleic Acid Binding—Sodium salt of oleic acid (Sigma-Aldrich) was coupled to EAH-Sepharose (Amersham Biosciences) by 1-ethyl-3-(3-dimethylaminopropyl)-carbodiimide (Pierce) to prepare oleate-Sepharose according to Peters *et al.* (25). Oleic acid coupling was verified by binding bovine serum albumin and recombinant α-synuclein protein. Mock-Sepharose was prepared from EAH-Sepharose by blocking coupling ligand with 1 M acetic acid. For the binding assay, 200 ng of Microcon-filtered protein was incubated with oleate-Sepharose or mock-Sepharose in 400 μl of phosphate-buffered saline containing 0.1 mM EDTA at 37 °C for 30 min with agitation. Protein bound to Sepharose was settled on a spun column and washed extensively with phosphate-buffered saline. The bound protein was then eluted with 50% ethanol. Eluates were subjected to SDS-PAGE and Western blotting.

Transmission Electron Microscopy—SOD1 proteins (40 μM) were incubated at 37 °C for 24 h in 50 mM phosphate buffer (pH 7.2) containing 150 mM NaCl and 0.1 mM EDTA supplemented with 100 μM arachidonic acid. The samples were absorbed to a glow-charged supporting membrane on 400-mesh grids and fixed by floating on 2.5% glutaraldehyde and 4% paraformaldehyde in 0.1 M phosphate buffer for 5 min. After three washes with distilled water, samples were negatively stained by 2% sodium phosphotungstic acid and dried. Specimens were observed in a LEO 912AB electron microscope (LEO Electron Microscopy), operated at 100 kV.

Toxicity Assay—Cytotoxicity of protein aggregates was measured as described previously (26, 27). In brief, neuro2a mouse neuroblastoma cells were maintained in Dulbecco's modified Eagle's medium with 10% fetal bovine serum and 2 mM glutamine in 5% CO_2 at 37 °C. Cells were differentiated in serum-free Dulbecco's modified Eagle's medium with 0.3 mM dibutylyl cAMP before use. Cells were plated at 30,000 cells/well in 96-well plates and differentiated overnight. The medium was removed, and prepared SOD1 aggregates were added in new medium without phenol red. After incubation for 18 h at 37 °C, the cells were assayed using an MTS reduction assay kit (Promega). Another plate also treated as described above was stained for 1 min with trypan blue, and stained cells were counted as dead cells.

RESULTS

Unsaturated Fatty Acids Promote Self-assembly of SOD1s—We expressed and homogeneously purified recombinant human SOD1s from the bacterial expression system (Fig. 1*A*). The purified wild-type and G93A enzymes showed comparable specific activity; however, A4V mutant showed ~56% activity compared with that of wild-type enzyme (Fig. 1*B*). The zinc ion content of the purified enzymes showed almost full occupancy; however, copper ion content of A4V was 54.5% of the wild-type level (Fig. 1*C*). Specific activity was correlated with copper ion occupancy of purified enzyme, indicating proper metal loading in the active site.

We next examined the effect of long-chain FAs on oligomerization of SOD1 proteins. Wild-type and mutant (A4V and G93A) SOD1 were incubated with various concentrations of arachidonic acid (AA) as described under "Experimental Procedures." After incubation, oligomerized SOD1 was subjected to SDS-PAGE and then detected by Western blotting. Under reducing conditions, mainly bands of ~16 and 38 kDa, corresponding to monomer and dimmer sizes of SOD1, respectively, were detected (Fig. 2*A*). In contrast, under non-reducing conditions, smeared patterns of >50 kDa in size were supposed to be SOD1 oligomers (Fig. 2*A*). These observations suggest that disulfide bonds maintained SOD1 oligomers. Thus, non-reducing SDS-PAGE was thought to be an efficient method to detect SOD1 oligomers and aggregates. Among the holo-enzymes, wild-type and G93A were not oligomerized; instead, they segregated as monomer and dimer size bands (Fig. 2*B*, *top panel*). After incubation with >100 μM AA, holo-A4V showed a faint smear pattern that was seen from 50 kDa to near the stacking gel range beside monomer- and dimer-size bands (Fig. 2*B*, *top panel*). In contrast, all metal-deficient enzymes, regardless of mutations, were oligomerized in the presence of >30 μM AA

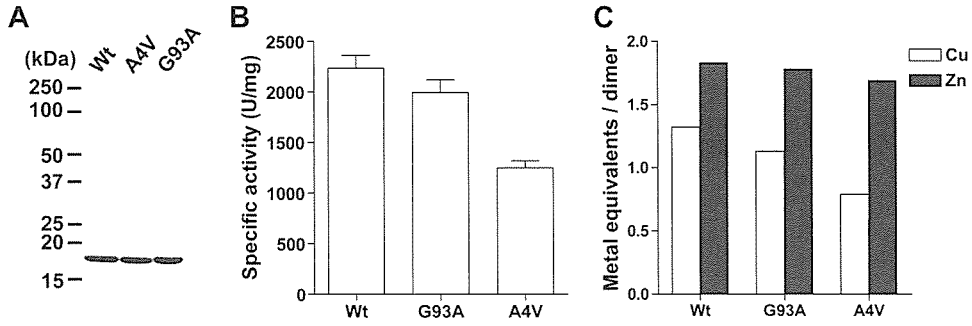

FIG. 1. **Characterization of purified recombinant SOD1s.** *A*, purified SOD1s were separated using SDS-PAGE and stained with Coomassie Brilliant Blue. *B*, dismutase activity of the purified SOD1s was assayed by the xanthine/xanthine oxidase-based method. One unit of the activity is defined as the amount of enzyme needed to exhibit 50% of dismutation of the superoxide radicals. *C*, metal content of the purified SOD1s was measured using 4-pyridylazoresorcinol assay in 6 M guanidine-HCl.

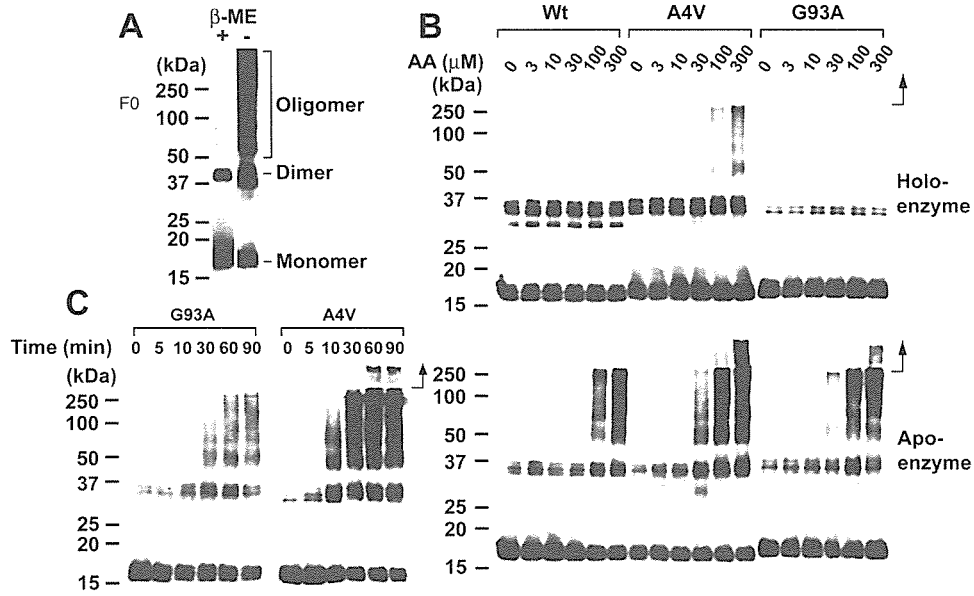

FIG. 2. **Arachidonic acid promotes SOD1 oligomerization.** *A*, FA-inducing oligomers of SOD1 were separated using SDS-PAGE with or without β-mercaptoethanol. *B*, apo-enzymes of SOD1 mutants (2.5 μM) were incubated at 37 °C in the presence of 100 μM AA. At each time point, aliquots were placed on ice to stop the reaction. *C*, purified holo- or apo-SOD1 proteins (2.5 μM) were incubated at 37 °C for 90 min in the presence of the indicated AA concentration. Incubated proteins were mixed directly with SDS-PAGE treatment buffer without reducing agents and boiled. SDS-PAGE was performed under non-reducing conditions. Proteins were detected by Western blotting as described under "Experimental Procedures." *Arrows* indicate the position of stacking gels.

(Fig. 2*B*, *bottom panel*). Apo-enzymes demonstrated higher oligomerization propensity than holo-enzymes depending on AA concentration (Fig. 2*B*). Thus, AA efficiently promoted oligomerization of SOD1s.

Next, we performed a time-course analysis of SOD1 oligomerization in the presence of AA. Metal-deficient G93A and A4V were oligomerized in a time-dependent manner (Fig. 2*C*). Maximum oligomerization was reached within 60 min of incubation in the presence of AA (Fig. 2*C*).

We then examined the effect that various FAs, including stearic acid, oleic acid, linoleic acid, and AA, have on SOD1 oligomerization. Unsaturated FAs, including oleic acid, linoleic acid, and AA, promoted SOD1 oligomerization (Fig. 3). However, saturated FAs and stearic acid had little effect on SOD1 oligomerization (Fig. 3). SOD1 oligomerization induced by FAs required at least monounsaturated FAs. This result may reflect the difference of solubility between unsaturated and saturated FAs in the buffer.

We verified the formation of SOD1 oligomers using a 10–40% glycerol density gradient centrifugation because presumable artifacts after detection of SOD1 oligomers using non-reducing SDS-PAGE may have remained. After fractionation, we could not observe high molecular mass SOD1 oligomers

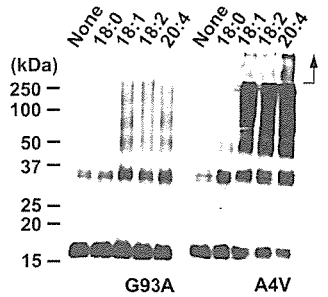

FIG. 3. **Unsaturated fatty acids affect oligomerization of SOD1.** Apo-enzymes of SOD1 mutants were incubated at 37 °C for 90 min in the presence of FAs at concentrations of 100 μM: 18:0, stearic acid; 18:1, oleic acid; 18:2, linoleic acid; and 20:4, arachidonic acid. *Arrows* indicate the position of stacking gels.

from the incubated sample in the absence of AA; fractions were <67 kDa and potentially represented monomer and dimer states (Fig. 4*A*, *top panel*). In contrast, we detected high molecular mass oligomers in fractions of >440 kDa from the incubated sample in the presence of AA (Fig. 4*A*, *bottom panel*). Under these conditions, SOD1 with molecular mass of <67 kDa was dramatically decreased compared with the sample incu-

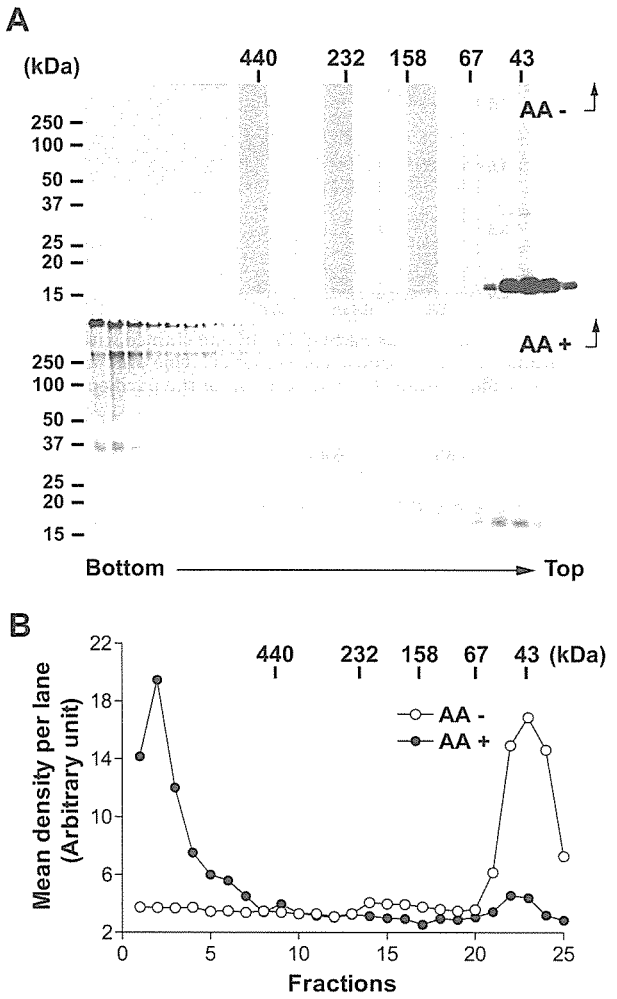

FIG. 4. **Glycerol density gradient centrifugation and densitometric analysis of SOD1 oligomers.** *A*, apo-A4V (2.5 μM) was incubated at 37 °C for 90 min in the absence or presence of 100 μM AA before loading on the glycerol cushion. After centrifugation, fractions were collected from the bottom of the tubes and then subjected to SDS-PAGE under non-reducing conditions. SOD1 proteins were detected by Western blotting. *B*, for densitometric analysis, we measured mean density per lane after background subtraction. Total mean density was similar under each condition, by calculating the mean density of visible lanes (*lanes 1–8* for oligomers and *lanes 21–25* for dimer or monomer). *Arrows* indicate the position of stacking gels.

bated in the absence of AA (Fig. 4*A*, *bottom panel*). Although oligomers of >440 kDa were fractionated by the glycerol density gradient centrifugation, these were detected as monomer, dimer, and smeared high molecular mass bands that reached stacking gels under non-reducing SDS-PAGE (Fig. 4*A*, *bottom panel*). This indicates oligomers are partly disrupted during the boiling of the SDS-PAGE loading buffer. We next performed densitometric analysis from Western blotting images to estimate the amount of oligomerized SOD1 (Fig. 4*B*). The resulting image analysis found that immunoreactivity for oligomers was ~80% of the total immunoreactivity.

Structural Instability of SOD1 Is Correlated to Oligomerization Propensity and FA Binding—We showed the FA-induced oligomerization propensity of apo-SOD1s was higher than that of holo-SOD1. This implies that protein stability might be strongly associated with FA-induced oligomerization propensity. Among the holo-enzymes, wild-type and G93A were not oligomerized under our experimental conditions (Fig. 2*B*, *top panel*). To examine the correlation between oligomerization propensity and protein stability of holo-enzymes, holo-SOD1 was heated and then oligomerized by AA. In the absence of AA,

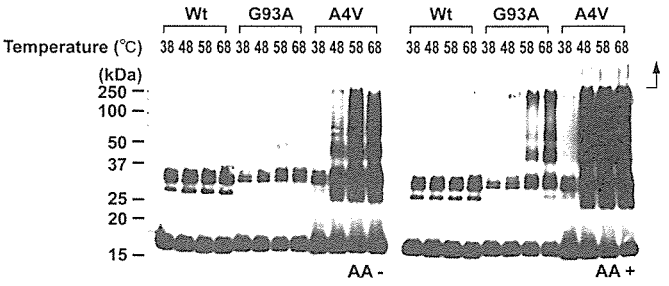

FIG. 5. **Thermally destabilized SOD1 mutants show a high oligomerization propensity.** Holo-enzymes were heat-treated at the indicated temperatures for 30 min before addition of 100 μM AA and then further incubated at 37 °C for 1 h. SDS-PAGE was performed under non-reducing conditions. Proteins were detected by Western blotting as described under "Experimental Procedures." *Arrows* indicate the position of stacking gels.

only heat-treated A4V was oligomerized (Fig. 5, *left panel*). In the presence of AA, heat-treated G93A and A4V were highly aggregated, but under the same conditions, wild-type SOD1 was not (Fig. 5, *right panel*). Oligomerization was observed above 58 °C for G93A and above 48 °C for A4V (Fig. 5, *right panel*). In the previous study, A4V was more unstable than G93A for heat treatment analyzed by differential scanning calorimetry (12). This result suggests that structural instability is strongly correlated with oligomerization propensity induced by FAs.

Although we showed that FAs promoted SOD1 oligomerization, the mechanism is not perfectly understood. Similarly, unsaturated FAs oligomerize α-synuclein and tau. In the case of α-synuclein and tau, FAs were bound to proteins, which suggested that oligomerization mechanisms underlie the FA binding characteristics of protein. To examine whether SOD1 binds to FAs, we carried out a solid-phase oleic acid binding assay. Among the holo-enzymes, very small amounts of holo-A4V were bound to the oleate-Sepharose column, whereas wild-type and G93A were not (Fig. 6*A*). All of the apo-enzymes were bound to oleate-Sepharose, regardless of their mutations (Fig. 6*A*). In contrast, bound proteins were not observed in mock-Sepharose (Fig. 6*A*). Nearly all of the input amounts of metal-deficient proteins were bound, which was estimated by 50% input. This finding suggests that metal-deficient SOD1 proteins strongly bind to FAs. We next examined whether heat-treated holo-enzymes bind to FAs. Apo-enzymes were used as control binding. Heat-treated SOD1 mutant (G93A) at 58 °C and 68 °C was bound to FAs, whereas wild-type was not (Fig. 6*B*). The results of the FA binding assay were strongly correlated with the oligomerization propensity of SOD1. These findings suggest that FA binding alters the conformation of SOD1 to form oligomers.

FA-induced SOD1 Aggregates Result in Granular Morphology and Are Cytotoxic—We analyzed the ultrastructure of SOD1 aggregates by electron microscope. SOD1 proteins (~40 μM) were incubated in the presence of 100 μM AA at 37 °C for 24 h. Holo-enzymes were heated at 50 °C for 30 min before incubation in the presence of AA. After incubation, granular aggregates were observed in all of apo-enzymes and heat-treated SOD1 mutants (Fig. 7*A*). In contrast, no visible materials were found in wild-type holo-SOD1s, even though they were heat-treated (Fig. 7*A*). The morphology of the aggregates was round or amorphous large granules composed of clustered small granules (Fig. 7*A*). We could not observe any visible protein aggregates in the samples incubated without AA, except in apo-A4V, which revealed a fibril structure (data not shown).

We next examined the effect of FA-induced aggregates on cell

viability of differentiated neuro2a cells. Aggregates of SOD1s were formed using the same methods as described for observation under an electron microscope. Aliquots incubated in the presence or absence of AA were diluted in the culture medium, which was directly added to differentiated neuro2a cells. After incubation for 18 h, toxicity was assessed with MTS reduction (Fig. 7*B*) and trypan blue staining (Fig. 7*C*). The presence of the granular aggregates formed by AA from Apo-SOD1s and heat-treated SOD1 mutants significantly reduced cell viability (Fig. 7, *B* and *C*). In contrast, no significant decrease of viability was detected when the cells were exposed either to incubated proteins in the absence of AA or to the buffer solutions used to form the aggregates in the absence of added protein (Fig. 7, *B* and *C*). These findings suggest that FA-induced SOD1 aggregates were highly toxic to the cells.

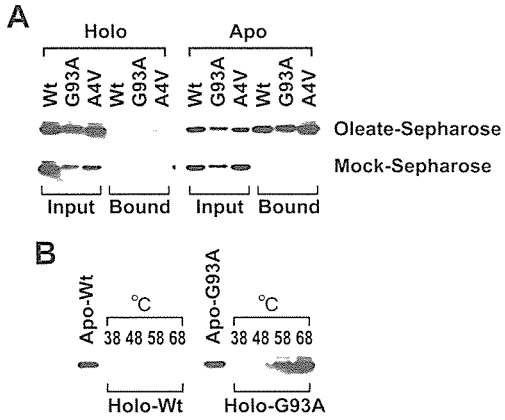

FIG. 6. **Solid-phase oleic acid binding assay shows apo-SOD1 or thermally destabilized SOD1 bound to oleate-Sepharose.** *A*, solid-phase binding assay was performed as described under "Experimental Procedures." Approximately 50% input (100 ng of proteins) was electrophoresed to estimate the quantity of FA binding SOD1. *B*, holo-SOD1s (wild-type and G93A) were thermally destabilized at the indicated temperatures for 30 min and then directly loaded on oleate-Sepharose. Apo-enzymes were used as positive controls for oleic acid binding.

DISCUSSION

Numerous neurodegenerative diseases are accompanied by highly insoluble inclusions of protein aggregates within characteristic neuronal populations. In the case of FALS, the protypical Lewy body-like hyaline inclusions, composed largely of granule-coated fibrils of SOD1-insoluble filaments, have been detected in the spinal cord of FALS patients with SOD1 gene mutations (5, 28). Although there has been controversy about whether such inclusions are a cause or a consequence of the neuronal degeneration, accumulating evidence suggests that aggregates formed via misfolded proteins, especially soluble oligomeric assemblies, may cause cell injury (29–31). Moreover, cytotoxicity of protein aggregates may have common features because granular aggregates form non-pathological proteins that can also be toxic (26). These findings suggest the avoidance of protein aggregation may be crucial for therapy of

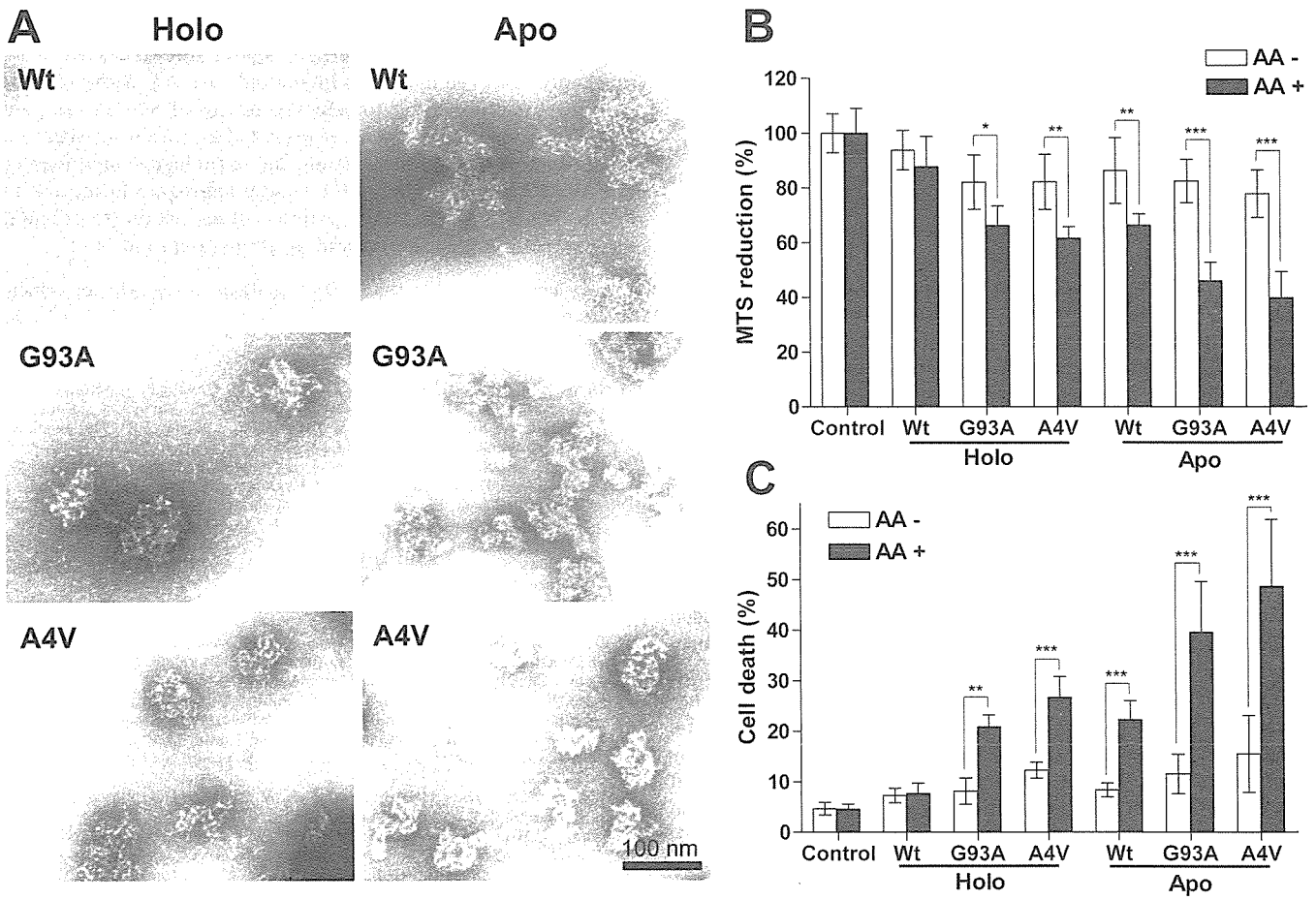

FIG. 7. **SOD1 aggregates and their cytotoxicity for the differentiated neuro2a cells.** Holo-SOD1s were pre-heated at 50 °C for 30 min before incubation with AA. SOD1 proteins (40 μM) were incubated in the presence of 100 μM AA at 37 °C for 24 h before observation under an electron microscope (*A*). Differentiated neuro2a cells were directly exposed for 18 h in medium containing incubated aliquots of SOD1s with or without arachidonic acid. The concentration of SOD1 in the culture medium was 4 μM. Buffer and AA carryover in the culture medium was controlled. Cytotoxicity was assessed using an MTS reduction assay (*B*) and trypan blue exclusion staining (*C*). The results were analyzed by two-way analysis of variance. The values are the means ± S.D. ($n = 6$). *, $p < 0.05$; **, $p < 0.01$; ***, $p < 0.001$.

conformational diseases including FALS.

In the present study, we demonstrated that unsaturated FAs promoted SOD1 oligomerization at physiological pH. SOD1 oligomers were detected by SDS-PAGE under non-reducing conditions. Although immunoreactivity for SOD1 oligomers was decreased in SDS-PAGE under reducing conditions, SOD1 oligomers were considerably SDS-resistant under non-reducing conditions. Based on this method, we found that apo-SOD1 proteins were highly oligomerized by AA compared with holo-SOD1 proteins in time-dependent and FA concentration-dependent manners (Fig. 2, *B* and *C*). Metal-deficient SOD1s may be representative of misfolding intermediates for their oligomeric assemblies because they are oligomerized independent of their mutations. These findings suggest that metal-deficient SOD1 proteins have a high oligomerization propensity, which is consistent with previous studies (9, 10, 13, 32). Moreover, heating of holo-SOD1 mutants increased the tendency to form oligomer complexes, especially in the presence of AA; however, the wild-type holo-SOD1 did not form oligomers, even after heating to 68 °C and exposure to AA (Fig. 5). This finding suggests that mutations of SOD1 primarily affect their conformation. Our time-course analysis of oligomerization demonstrates that FAs induced the oligomerization process fairly rapidly. We could detect oligomers within 1 h of incubation in the presence of AA (Fig. 1*C*). Glycerol density gradient centrifugation analysis showed that oligomer species were roughly estimated to be >80% of the total SOD1 after a 90-min incubation in the presence of AA (Fig. 4). The conversion efficiency and the speed of oligomer formation may be considered as supportive evidence that these reactions occur *in vivo*.

Aggregations of misfolded proteins are primarily affected by their mutations, especially in inherited conformational diseases. Mutant proteins in conformational diseases have a common characteristic of easily unfolding in a physiological condition and favoring aggregate formation. Protein aggregation has also been shown to be modulated by several factors, including protein concentration, pH, and interactions with other elements such as lipid molecules. It has been reported that FAs stimulated the polymerization of amyloid β-peptides, tau (17, 33), and α-synuclein (18, 19) *in vitro*. These studies suggest that FAs play a pivotal role as nucleates in the self-assembly of misfolded proteins. Although the precise mechanism of how lipid molecules accelerate protein aggregation has not been elucidated, it has been proposed that lipid-bound proteins change their conformation or anionic surfaces, presenting as micelles or vesicles, which can serve to nucleate aggregate formation (18, 34, 35). We confirmed that apo-SOD1s or heat-treated holo-SOD1 mutants were bound to oleic acid (Fig. 6). The FA binding properties of SOD1s were strongly correlated to their conformational instability. These results are consistent with the notion that misfolding intermediates of SOD1 caused by mutations or metal loss may be facilitated by FAs to form oligomeric structures. Another possible mechanism is protein oxidation by FAs. Oxidation also enhances misfolding and aggregation of SOD1 (32). In particular, FAs can lead to the production of radicals because they are easily peroxidized by auto-oxidation to generate peroxyl radicals. However, we could not inhibit SOD1 oligomerization using even a considerable amount of radical scavenger (data not shown). Moreover, oxidized derivatives of FAs also induced SOD1 oligomerization to a similar extent with fresh FAs (data not shown). This finding suggests that oxidation or oxidative damage of SOD1 does not directly drive SOD1 oligomerization. Rather, it is most likely to be associated with a SOD1-destabilizing event.

Recently, several studies for *in vitro* aggregation of SOD1 have been published. Aggregation of SOD1 can be induced by metal-catalyzed oxidation (32), trifluoroethanol, or heat treatment (10), which induces oxidative modification or protein destabilization. This indicates that structurally unstable SOD1 has an influence on its aggregate formation *in vitro*. Crystallographic studies suggest that metal-deficient SOD1 forms an amyloid-like assembly caused by non-native conformational changes and permits dimer interaction (36, 37). This amyloid-like structure was represented by prolonged incubation of SOD1 at acidic pH (9). In the present study, ultrastructural analysis showed that the FA-inducing aggregates had round or amorphous morphology with clustered tiny spherical aggregates (Fig. 7*A*). They resemble pre-fibrillar aggregates of the N-terminal domain of *Escherichia coli* HypF protein or aggregates of the Src homology 3 domain of cytosolic phosphatidylinositol 3-kinase as reported by Stefani and co-workers (26). They demonstrated that granular aggregates of proteins, even non-pathological proteins, are cytotoxic when applied externally (26). Our data also demonstrate that granular aggregates of SOD1s reveal significant cytotoxicity (Fig. 7, *B* and *C*). Although the cytotoxic mechanism of the aggregates is not completely understood, it has been proposed that such pre-fibrillar intermediates may lead to cytotoxicity by permeabilization of the membrane bilayer (38, 39).

The present findings may provide considerable pathological implication for FALS. Lipid molecules such as FAs may be positive modulators for misfolded protein aggregations. Most misfolded proteins including SOD1 mutants are rapidly degraded by the ubiquitin-proteasome system. Unsaturated FAs may promote misfolded protein aggregations before they are degraded. In addition, cytotoxic aggregate formation of SOD1 may require FAs because granular aggregates structures were markedly observed in SOD1s incubated with AA. Although it is not clear whether the cytotoxic aggregates of SOD1s are generated intracellularly, we have provided a protein aggregation model system to help understand the pathological significance of FAs as a positive modulator for the aggregate formation in FALS. We believe that our system will contribute to efficient drug screening for inhibitors of SOD1 aggregation.

Acknowledgment—We thank Dr. Toshihide Kobayashi for critical advice and helpful discussions.

REFERENCES

1. Deng, H. X., Hentati, A., Tainer, J. A., Iqbal, Z., Cayabyab, A., Hung, W. Y., Getzoff, E. D., Hu, P., Herzfeldt, B., Roos, R. P., Warner, C., Deng, G., Soriano, E., Smyth, C., Parge, H. E., Ahmed, A., Roses, A. D., Hallewell, R., Pericak-Vance, M. A., and Siddique, T. (1993) *Science* **261,** 1047–1051
2. Rosen, D. R., Siddique, T., Patterson, D., Figlewicz, D. A., Sapp, P., Hentati, A., Donaldson, D., Goto, J., O'Regan, J. P., Deng, H. X., Rahmani, Z., Krizus, A., McKenna-Yasek, D., Cayabyab, A., Gaston, S., Tanzi, R., Halperin, J. J., Herzfeldt, B., Van den Berg, R., Hung, W., Bird, T., Deng, G., Mulder, D. W., Smith, C., Laing, N. G., Soriano, E., Pericak-Vance, M. A., Haines, J., Rouleau, G. A., Gusella, J., Horvitz, H. R., and Brown, R. H., Jr. (1993) *Nature* **362,** 59–62
3. Shibata, N., Asayama, K., Hirano, A., and Kobayashi, M. (1996) *Dev. Neurosci.* **18,** 492–498
4. Bruijn, L. I., Becher, M. W., Lee, M. K., Anderson, K. L., Jenkins, N. A., Copeland, N. G., Sisodia, S. S., Rothstein, J. D., Borchelt, D. R., Price, D. L., and Cleveland, D. W. (1997) *Neuron* **18,** 327–338
5. Kato, S., Hayashi, H., Nakashima, K., Nanba, E., Kato, M., Hirano, A., Nakano, I., Asayama, K., and Ohama, E. (1997) *Am. J. Pathol.* **151,** 611–620
6. Shibata, N., Hirano, A., Kobayashi, M., Dal Canto, M. C., Gurney, M. E., Komori, T., Umahara, T., and Asayama, K. (1998) *Acta Neuropathol.* **95,** 136–142
7. Watanabe, M., Dykes-Hoberg, M., Culotta, V. C., Price, D. L., Wong, P. C., and Rothstein, J. D. (2001) *Neurobiol. Dis.* **8,** 933–941
8. Wang, J., Xu, G., Gonzales, V., Coonfield, M., Fromholt, D., Copeland, N. G., Jenkins, N. A., and Borchelt, D. R. (2002) *Neurobiol. Dis.* **10,** 128–138
9. DiDonato, M., Craig, L., Huff, M. E., Thayer, M. M., Cardoso, R. M., Kassmann, C. J., Lo, T. P., Bruns, C. K., Powers, E. T., Kelly, J. W., Getzoff, E. D., and Tainer, J. A. (2003) *J. Mol. Biol.* **332,** 601–615
10. Stathopulos, P. B., Rumfeldt, J. A., Scholz, G. A., Irani, R. A., Frey, H. E., Hallewell, R. A., Lepock, J. R., and Meiering, E. M. (2003) *Proc. Natl. Acad. Sci. U. S. A.* **100,** 7021–7026
11. Hayward, L. J., Rodriguez, J. A., Kim, J. W., Tiwari, A., Goto, J. J., Cabelli, D. E., Valentine, J. S., and Brown, R. H., Jr. (2002) *J. Biol. Chem.* **277,** 15923–15931

12. Rodriguez, J. A., Valentine, J. S., Eggers, D. K., Roe, J. A., Tiwari, A., Brown, R. H., Jr., and Hayward, L. J. (2002) *J. Biol. Chem.* **277,** 15932–15937
13. Lindberg, M. J., Tibell, L., and Oliveberg, M. (2002) *Proc. Natl. Acad. Sci. U. S. A.* **99,** 16607–16612
14. Johnston, J. A., Dalton, M. J., Gurney, M. E., and Kopito, R. R. (2000) *Proc. Natl. Acad. Sci. U. S. A.* **97,** 12571–12576
15. Urushitani, M., Kurisu, J., Tateno, M., Hatakeyama, S., Nakayama, K., Kato, S., and Takahashi, R. (2004) *J. Neurochem.* **90,** 231–244
16. Shinder, G. A., Lacourse, M. C., Minotti, S., and Durham, H. D. (2001) *J. Biol. Chem.* **276,** 12791–12796
17. Wilson, D. M., and Binder, L. I. (1997) *Am. J. Pathol.* **150,** 2181–2195
18. Sharon, R., Goldberg, M. S., Bar-Josef, I., Betensky, R. A., Shen, J., and Selkoe, D. J. (2001) *Proc. Natl. Acad. Sci. U. S. A.* **98,** 9110–9115
19. Sharon, R., Bar-Joseph, I., Frosch, M. P., Walsh, D. M., Hamilton, J. A., and Selkoe, D. J. (2003) *Neuron* **37,** 583–595
20. Urushitani, M., Kurisu, J., Tsukita, K., and Takahashi, R. (2002) *J. Neurochem.* **83,** 1030–1042
21. Fried, R. (1975) *Biochimie (Paris)* **57,** 657–660
22. Crow, J. P., Sampson, J. B., Zhuang, Y., Thompson, J. A., and Beckman, J. S. (1997) *J. Neurochem.* **69,** 1936–1944
23. Boissinot, M., Karnas, S., Lepock, J. R., Cabelli, D. E., Tainer, J. A., Getzoff, E. D., and Hallewell, R. A. (1997) *EMBO J.* **16,** 2171–2178
24. Bartnikas, T. B., and Gitlin, J. D. (2003) *J. Biol. Chem.* **278,** 33602–33608
25. Peters, T., Jr., Taniuchi, H., and Anfinsen, C. B., Jr. (1973) *J. Biol. Chem.* **248,** 2447–2451
26. Bucciantini, M., Giannoni, E., Chiti, F., Baroni, F., Formigli, L., Zurdo, J., Taddei, N., Ramponi, G., Dobson, C. M., and Stefani, M. (2002) *Nature* **416,** 507–511
27. Kayed, R., Head, E., Thompson, J. L., McIntire, T. M., Milton, S. C., Cotman, C. W., and Glabe, C. G. (2003) *Science* **300,** 486–489
28. Kato, S., Saito, M., Hirano, A., and Ohama, E. (1999) *Histol. Histopathol.* **14,** 973–989
29. Walsh, D. M., Hartley, D. M., Kusumoto, Y., Fezoui, Y., Condron, M. M., Lomakin, A., Benedek, G. B., Selkoe, D. J., and Teplow, D. B. (1999) *J. Biol. Chem.* **274,** 25945–25952
30. Hartley, D. M., Walsh, D. M., Ye, C. P., Diehl, T., Vasquez, S., Vassilev, P. M., Teplow, D. B., and Selkoe, D. J. (1999) *J. Neurosci.* **19,** 8876–8884
31. Tateno, M., Sadakata, H., Tanaka, M., Itohara, S., Shin, R. M., Miura, M., Masuda, M., Aosaki, T., Urushitani, M., Misawa, H., and Takahashi, R. (2004) *Hum. Mol. Genet.* **13,** 2183–2196
32. Rakhit, R., Cunningham, P., Furtos-Matei, A., Dahan, S., Qi, X. F., Crow, J. P., Cashman, N. R., Kondejewski, L. H., and Chakrabartty, A. (2002) *J. Biol. Chem.* **277,** 47551–47556
33. Gamblin, T. C., King, M. E., Kuret, J., Berry, R. W., and Binder, L. I. (2000) *Biochemistry* **39,** 14203–14210
34. Necula, M., Chirita, C. N., and Kuret, J. (2003) *J. Biol. Chem.* **278,** 46674–46680
35. Chirita, C. N., Necula, M., and Kuret, J. (2003) *J. Biol. Chem.* **278,** 25644–25650
36. Elam, J. S., Taylor, A. B., Strange, R., Antonyuk, S., Doucette, P. A., Rodriguez, J. A., Hasnain, S. S., Hayward, L. J., Valentine, J. S., Yeates, T. O., and Hart, P. J. (2003) *Nat. Struct. Biol.* **10,** 461–467
37. Strange, R. W., Antonyuk, S., Hough, M. A., Doucette, P. A., Rodriguez, J. A., Hart, P. J., Hayward, L. J., Valentine, J. S., and Hasnain, S. S. (2003) *J. Mol. Biol.* **328,** 877–891
38. Caughey, B., and Lansbury, P. T. (2003) *Annu. Rev. Neurosci.* **26,** 267–298
39. Kayed, R., Sokolov, Y., Edmonds, B., McIntire, T. M., Milton, S. C., Hall, J. E., and Glabe, C. G. (2004) *J. Biol. Chem.* **279,** 46363–46366

Inactivation of *Drosophila* DJ-1 leads to impairments of oxidative stress response and phosphatidylinositol 3-kinase Akt signaling

Yufeng Yang*†, Stephan Gehrke*†, Md. Emdadul Haque*, Yuzuru Imai*, Jon Kosek*, Lichuan Yang‡, M. Flint Beal‡, Isao Nishimura§, Kazumasa Wakamatsu¶, Shosuke Ito¶, Ryosuke Takahashi, and Bingwei Lu*,**

*Department of Pathology, Stanford University School of Medicine, and Geriatric Research, Education and Clinical Center Veterans Affairs Palo Alto Health Care System, Palo Alto, CA 94304; ‡Department of Neurology, Cornell University Medical College, 525 East 68th Street, New York, NY 10021; §Division of Regulation of Macromolecular Functions, Institute for Protein Research, Osaka University, 3-2 Yamadaoka, Suita, Osaka 565-0871, Japan; ¶Department of Chemistry, Fujita Health University School of Health Sciences, Toyoake, Aichi 470-1192, Japan; and Laboratory for Motor System Neurodegeneration, RIKEN Brain Science Institute, 2-1 Hirosawa, Wako-shi, Saitama 351-0198, Japan

Edited by Tak Wah Mak, University of Toronto, Toronto, Canada, and approved July 29, 2005 (received for review June 3, 2005)

Parkinson's disease (PD) is the most common movement disorder characterized by dopaminergic dysfunction and degeneration. The cause of most PD cases is unknown, although postmortem studies have implicated the involvement of oxidative stress. The identification of familial PD-associated genes offers the opportunity to study mechanisms of PD pathogenesis in model organisms. Here, we show that DJ-1A, a *Drosophila* homologue of the familial PD-associated gene DJ-1, plays an essential role in oxidative stress response and neuronal maintenance. Inhibition of DJ-1A function through RNA interference (RNAi) results in cellular accumulation of reactive oxygen species, organismal hypersensitivity to oxidative stress, and dysfunction and degeneration of dopaminergic and photoreceptor neurons. To identify other genes that may interact with DJ-1A in regulating cell survival, we performed genetic interaction studies and identified components of the phosphatidylinositol 3-kinase (PI3K) Akt-signaling pathway as specific modulators of DJ-1A RNAi-induced neurodegeneration. PI3K signaling suppresses DJ-1A RNAi phenotypes at least in part by reducing cellular reactive oxygen species levels. Consistent with the genetic interaction results, we also found reduced phosphorylation of Akt in DJ-1A RNAi animals, indicating an impairment of PI3K Akt signaling by DJ-1A down-regulation. Together with recent findings in mammalian systems, these results implicate impairments of PI3K Akt signaling and oxidative stress response in DJ-1-associated disease pathogenesis. We also observed impairment of PI3K Akt signaling in the fly *parkin* model of PD, hinting at a common molecular event in the pathogenesis of PD. Manipulation of PI3K Akt signaling may therefore offer therapeutic benefits for the treatment of PD.

Parkinson's disease PI3K PTEN Akt signaling reactive oxygen species

Parkinson's disease (PD) is the most common movement disorder and the second most common neurodegenerative disease. The movement abnormality in PD arises from deficiency of brain dopamine (DA) contents and the degeneration of dopaminergic neurons in the substantia nigra. The most common forms of PD are sporadic with no known cause. Nevertheless, postmortem studies have identified common features associated with sporadic PD, including defects in mitochondrial complex I function, oxidative damage, and abnormal protein aggregation (1).

The contribution of genetic factors in the pathogenesis of PD, although initially controversial, has been firmly established by recent human genetic studies. At least 10 distinct loci (PARK1 to -11) have been linked to rare familial forms of PD (2). It is anticipated that understanding the molecular lesions associated with these familial PD (FPD) genes will shed light on the pathogenesis of the sporadic forms of the disease. To date, five unequivocal FPD genes have been molecularly cloned. These include -*Synuclein* (-Syn), Parkin, DJ-1, PINK-1, and dardarin. Biochemical and biophysical studies of -Syn and Parkin have primarily linked dysfunction of these genes to aberrant protein folding and ubiquitin-proteasome dysfunction. Intriguingly, *in vivo* genetic and *in vitro* cell culture studies have revealed their connection to mitochondrial dysfunction and oxidative stress, reinforcing the involvement of these processes in PD pathogenesis in general (3).

DJ-1 encodes a conserved protein belonging to the ThiJ PfpI DJ-1 superfamily. The exact molecular function of DJ-1 is still unclear. Human DJ-1 was initially discovered as a candidate oncoprotein that could transform cells in cooperation with activated *ras* (4), and it was later found as a component of an RNA-binding protein complex and was associated with male infertility (4–6). Under oxidative stress conditions, DJ-1 was modified by oxidation, and the modified form associated with mitochondria in cultured cells (7–10). Knocking down DJ-1 expression with small interfering RNA (siRNA) resulted in susceptibility to oxidative stress, endoplasmic reticulum stress, and proteasome inhibition (11). Recent analyses of DJ-1 knockout mice have shed light on the physiological function of DJ-1 in mammals. DJ-1-deficient mice were found to have nigrostriatal dopaminergic dysfunction, motor deficits, and hypersensitivity to the neurotoxin 1-methyl-4-phenyl-1,2,3,6-tetrahydropyrindine (MPTP) and oxidative stress stimuli (12–14). In mammalian cells, DJ-1 was found to regulate the phosphorylation status of protein kinase B (PKB) Akt through the tumor suppressor PTEN (15). The relevance of this novel finding of DJ-1 function to PD pathogenesis remains to be explored.

As an alternative approach to understanding the role of DJ-1 dysfunction in PD pathogenesis, we have used *Drosophila* as a model system. We inhibited the function of a *Drosophila* DJ-1 homologue (DJ-1A) by transgenic RNA interference (RNAi). DJ-1A RNAi flies show cellular accumulation of reactive oxygen species (ROS), hypersensitivity to oxidative stress, and degeneration of dopaminergic and photoreceptor neurons. Genetic interaction studies with candidate genes and pathways previously implicated in survival signaling led to the identification of genes in the PI3K Akt-signaling pathway as specific modifiers of DJ-1A-associated cell death phenotype. Consistent with the genetic interaction results, PI3K signaling was found to regulate cellular ROS levels, and we found that DJ-1A down-regulation leads to impairment of PI3K Akt signaling. Significantly, we found that dysfunction of *parkin*, another PD-associated gene, also led to impaired

This paper was submitted directly (Track II) to the PNAS office.

Abbreviations: DA, dopamine; DMC, dorsomedial cluster; PD, Parkinson's disease; RNAi, RNA interference; ROS, reactive oxygen species; TH, tyrosine hydroxylase; PKB, protein kinase B; PI3K, phosphatidylinositol 3-kinase; *Da*, *daughterless*; 3-AT, 3-amino-triazole; DCFH-DA, 2,7-dichlorofluorescein diacetate; DN, dominant-negative.

†Y.Y. and S.G. contributed equally to this work.

**To whom correspondence should be addressed. E-mail: bingwei@stanford.edu.

PI3K Akt signaling. Our results implicate oxidative stress and impairment of PI3K Akt signaling as a general feature of PD pathogenesis and suggest new avenues for therapeutic intervention.

Experimental Procedures

***Drosophila* Genetics.** Fly culture and crosses were performed according to standard procedures and raised at indicated temperatures. All general fly stocks and *GAL4* lines were obtained from the Bloomington *Drosophila* Stock Center. The other fly stocks have been described: *UAS-Akt* (16); *UAS-PI3Kp110* and *UAS-PI3Kp110 DN* (17); *UAS-PTEN* (18); and *UAS-tau V337M* (19). To generate *UAS-dsDJ-1A* and *UAS-dsDJ-1B* transgenics, genomic DNA cDNA hybrid constructs were generated as described (20). To make *UAS-DJ-1A*, *UAS-DJ-1B*, and *UAS-hDJ-1* transgenics, corresponding full-length cDNA was cloned into the *pUAST* vector. Details of the cloning steps are available upon request. Approximately 9 g of *pUAST* transgenic construct was mixed with 3 g of helper plasmid in 20 1 of injection buffer. Standard procedures were followed for embryo injection and recovery of transgenic lines.

Molecular Biology. For RT PCR analysis, 2nd to 3rd instar larvae from the cross between *UAS-dsDJ-1A* and *Da-GAL4* were used to prepare total RNA by using an RNeasy Kit (Qiagen, Valencia, CA). Details of the quantitative RT PCR procedure were essentially as described (21). Antibodies against DJ-1A and DJ-1B were elicited in rabbits with recombinant proteins purified from bacteria culture expressing *pGEX-6P-1-DJ-1A* or *pGEX-6P-1-DJ-1B* vectors, which contain corresponding full-length cDNA inserts. Western blot analysis using these antibodies was performed as described (21), with each primary antibody used at 1:5,000 dilution. For Western blot analysis of Akt, *Da-GAL4* and *Da-GAL4 DJ-1A RNAi* animals were raised at 18°C from the larvae stage to obtain viable *Da-GAL4 DJ-1A RNAi* adult animals, because these animals die at larvae stage when raised at 25°C. Newly eclosed adult flies were transferred to 29°C to induce stronger RNAi. *Da-GAL4 dParkin RNAi* flies were raised at 29°C constantly. Fly head extracts were prepared for Western blot analysis with anti-Akt and anti-*p*-Akt (S505) antibodies (Cell Signaling Technology, Beverly, MA).

Histology and Immunohistochemistry. Sections of paraplast-embedded adult fly heads were prepared and processed as described (21). The sections were incubated in primary antibody overnight at 4°C, and subsequently processed by using the Vectastain Universal Elite ABC Kit (Vector Laboratories). The primary antibody used was anti-tyrosine hydroxylase (TH) polyclonal antibody (Pel-Freez Biologicals, 1:100). For the analysis of adult retina, eye sectioning and staining with toluidine blue was performed as described (22). Between four and five fly heads for each genotype per time point were examined, and each experiment was repeated at least once. The neuronal culture system was established and processed for immunofluorescence staining as described (21). For ROS staining of neuronal culture and adult fly brain, 2,7-dichlorofluorescein diacetate (DCFH-DA) (Molecular Probes) was used following the manufacturer's instructions.

DA Measurement. HPLC analysis of catecholamine levels was performed as described (23, 24). For sample preparation, adult male fly heads were dissected out and homogenized in 0.1 M perchloric acid (generally 50 1 per four or five heads) by using a motorized hand-held tissue grinder. The homogenate was frozen immediately on dry ice and stored at 80°C before HPLC analysis.

Oxidative Stress Assay. For oxidative stress assay, flies were kept in plastic vials with a piece of Kimwipe paper soaked with 1% H_2O_2 or 100 mM 3-amino-triazole (3-AT) in Schneider's Medium. The vials were kept at 25°C in a shielded box. Fresh H_2O_2 or 3-AT was added to the paper daily with a syringe. Mortality was recorded every 12 h or at shorter intervals.

Results

Specific Knockdown of *Drosophila DJ-1A* Expression by Transgenic RNAi. In the sequenced *Drosophila* genome, there are two previously uncharacterized genes, *CG6646* and *CG1349* (referred to as *DJ-1A* and *DJ-1B*, respectively), which are homologous to human *DJ-1*. Sequence alignment shows that DJ-1A contains the three conserved amino acids proposed to form a putative catalytic triad in human DJ-1 (25), whereas DJ-1B lacks one of the three amino acids. This finding suggests that DJ-1A may be more closely related to human DJ-1. As a first step toward addressing the function of DJ-1A in *Drosophila*, we used the transgenic RNAi approach to knockdown DJ-1A expression (20). To confirm that the expression of *DJ-1A* dsRNA resulted in a down-regulation of endogenous *DJ-1A* transcripts, we used quantitative RT-PCR to measure *DJ-1A* mRNA levels after ubiquitous induction of DJ-1A RNAi. A dramatic reduction of *DJ-1A* mRNA was observed, whereas *DJ-1B* mRNA was relatively unchanged (Fig. 1*A*). We next tested the effect of RNAi on endogenous DJ-1 protein expression using DJ-1A- and DJ-1B-specific antibodies. As shown in Fig. 1*B*, ubiquitous DJ-1A RNAi resulted in a significant reduction of endogenous DJ-1A protein expression on Western blots. In contrast, the level of DJ-1B protein was relatively unaffected. Taken together, these results show that RNAi causes a specific knockdown of DJ-1A RNA and protein expression.

Targeted Inhibition of DJ-1A in the Eye Results in Photoreceptor Loss. We next analyzed the physiological consequence of inhibiting DJ-1A function. Ubiquitous expression of *DJ-1A* dsRNA with *actin-GAL4* or *daughterless (Da)*-GAL4 resulted in larval lethality. This finding suggests that DJ-1A is an essential gene in *Drosophila*. To circumvent the lethality problem, we used well characterized GAL4 drivers to inhibit DJ-1A expression in specific tissues and cell types and at different stages. Induction of DJ-1A RNAi in the developing eye using *GMR-GAL4* driver produced a rough eye phenotype (Fig. 1 *D* and *H*). *GMR-GAL4* directs gene expression in postmitotic cells posterior to the morphogenetic furrow and a small group of premitotic cells in the developing eye. Staining of eye sections revealed loss of photoreceptor neurons in some ommatidia (Fig. 1*J*), indicating that the rough eye phenotype is caused at least in part by photoreceptor cell loss. This RNAi effect is dosage-dependent, because increasing the copy number of *GAL4* and *UAS* transgenes caused a more severe degeneration of the eye (Fig. 1*K*). Several lines of evidence suggest that this eye phenotype is caused by specific inhibition of DJ-1A. First, overexpression of *white* or *dParkin* control dsRNAs using the same *GAL4* driver had no effect on eye morphology (data not shown), suggesting that the eye phenotype was not due to a nonspecific effect of dsRNA expression. Second, in a *DJ-1A* heterozygous genetic background, the eye phenotype was significantly enhanced (Fig. 1*F*), consistent with the RNAi effect being dosage dependent. Finally, we could rescue the RNAi phenotype with increased expression of *DJ-1A*. Given that the RNAi effect is dosage-dependent, we reasoned that, by raising the basal level of *DJ-1A* transcripts, the RNAi effect would be dampened. Indeed, coexpression of *UAS-DJ-1A* transgenes partially suppressed the eye degeneration phenotype induced by strong RNAi (Fig. 1, compare *M* with *K*). Coexpression of a human DJ-1 transgene could also partially rescue (Fig. 1, compare *N* with *K*), suggesting that human DJ-1 and fly DJ-1A may possess similar properties. In contrast, coexpression of a *GFP* transgene had no effect (Fig. 1, compare *L* with *K*), suggesting that the rescue is not due to titration of GAL4 by added expression of a *UAS*-transgene. We conclude that the abnormal eye phenotype is specifically caused by inhibition of DJ-1A expression.

Inhibition of *DJ-1A* in Dopaminergic Neurons Leads to Decreases of TH Neuron Number and Brain DA Content. We next analyzed the effects of inhibiting DJ-1A function in dopaminergic neurons by

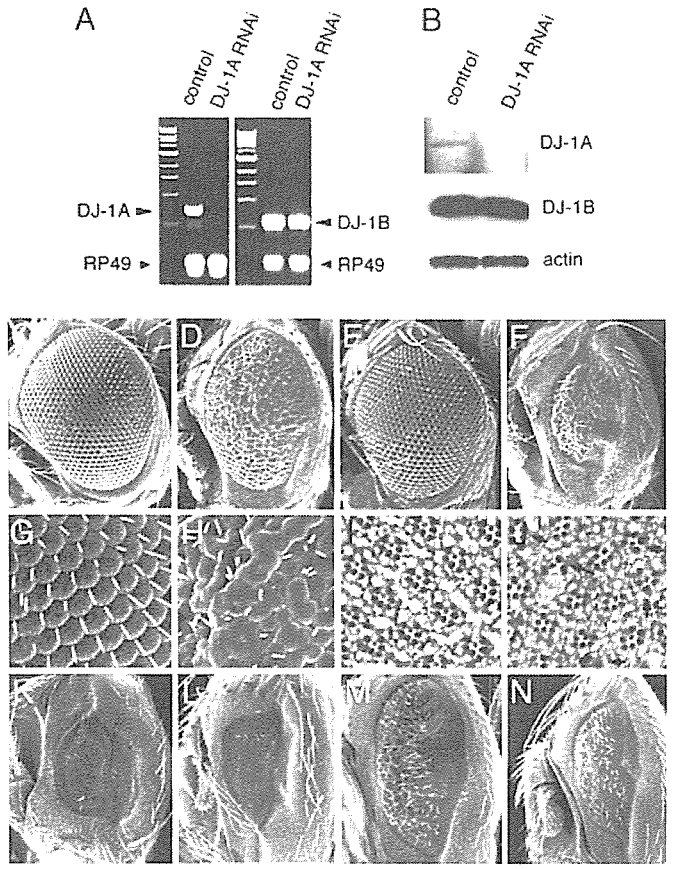

Fig. 1. Inhibition of *DJ-1A* expression by RNAi leads to photoreceptor neuron loss and eye degeneration. (*A*) Quantitative RT PCR analysis of *DJ-1A* mRNA level after RNAi. *DJ-1B* and *RP49* serve as controls. (*B*) Western blot analysis of DJ-1A protein level after RNAi. DJ-1B and actin serve as controls. (*C–H*) SEM images of *GMR-GAL4* (*C*), *GMR-GAL4 UAS-DJ-1A-RNAi* (*D*), *GMR-GAL4 Df(2R)CX1* (*E*), and *GMR-GAL4 UAS-DJ-1A-RNAi Df(2R)CX1* (*F*) eyes. *Df(2R)CX1* is a chromosomal deficiency that deletes *DJ-1A*. *G* and *H* are magnified views of *C* and *D*, respectively. (*I* and *J*) Staining of photoreceptor neurons in *GMR-GAL4* (*I*), and *GMR-GAL4 UAS-DJ-1A-RNAi* (*J*) eyes. Arrows in *J* mark ommatidia with photoreceptor loss. (*K–N*) Rescue of DJ-1A RNAi phenotypes by overexpressing *DJ-1A* or human *DJ-1*. All flies are homozygous for a recombinant *GMR-GAL4;UAS-DJ-1A-RNAi* chromosome and thus have a stronger phenotype than the one shown in *B*. In addition, the flies coexpress *UAS-GFP* (*L*), *UAS-DJ-1A* (*M*), *UAS-hDJ-1* (*N*), or no other transgene (*K*).

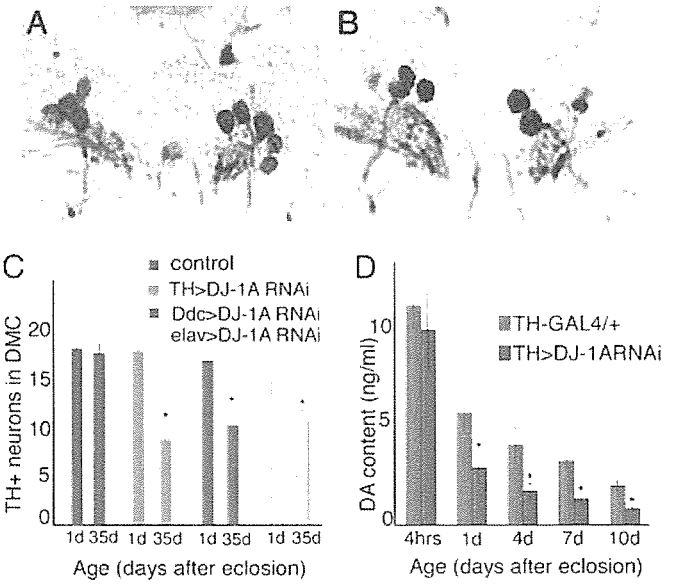

Fig. 2. Dopaminergic defects in *DJ-1A RNAi* flies. (*A* and *B*) TH immunostaining of DMC dopaminergic neurons in 35-day-old control *Ddc-GAL4* (*A*) and *Ddc-GAL4 DJ-1A RNAi* (*B*) male flies. Sections containing most of the DMC dopaminergic neurons are shown. (*C*) Quantification of TH neurons in the DMC of control flies and *DJ-1A RNAi* flies directed with *TH-GAL4*, *Ddc-GAL4*, or *elav-GAL4* drivers. The difference in cell count between 1-day-old and 35-day-old *DJ-1A RNAi* flies is significant. *, P 0.01 in Student's t test. (*D*) Quantification of head DA levels in *TH-GAL4* and *TH-GAL4 DJ-1A RNAi* flies. *, P 0.01 in Student's t test.

inducing RNAi with the *Ddc-GAL4* driver. We focused on the dopaminergic neurons in the dorsomedial clusters (DMC), which are known to be susceptible under disease conditions (26). Immunostaining of paraffin brain sections of *Ddc-GAL4 DJ-1A RNAi* flies revealed an age-dependent reduction in the number of TH neurons in the DMC. In 1-day-old flies, a normal complement of TH neurons (18) was present (Fig. 2*C*), but, in 35-day and older flies, only 10–12 of these neurons could be detected immunochemically (Fig. 2 *B* and *C*). Control flies showed no significant change in the number of these neurons during aging (Fig. 2 *A* and *C*). Induction of DJ-1A RNAi with another dopaminergic GAL4 driver, *TH-GAL4*, or the pan-neuronal *elav-GAL4* driver also resulted in reduction of TH neurons in the DM clusters (Fig. 2*C*).

To further confirm that loss of DJ-1A leads to dopaminergic dysfunction, we measured brain DA levels using head extracts prepared from control and *DJ-1A RNAi* flies. In newly eclosed flies, DA content was comparable between control and *RNAi* flies (Fig. 2*D*). However, 1 day after eclosion, *DJ-1A RNAi* flies showed significantly reduced DA level than control flies. At 4, 7, and 10 days of age, control and *DJ-1A RNAi* flies both showed age-dependent decline of DA, but *DJ-1A RNAi* flies consistently exhibited more reduction than the controls (Fig. 2*D*). Because a normal complement of TH dopaminergic neurons was present in 1-day old flies, the reduction of brain DA content at this early stage could not be attributed to neuronal loss. This result suggests that, in addition to promoting dopaminergic neuron survival, *Drosophila* DJ-1A may play an early role in regulating brain DA levels.

***DJ-1A RNAi* Flies Show Elevated ROS Accumulation and Hypersensitivity to Oxidative Stress.** We further characterized the *DJ-1A RNAi* animals to learn DJ-1A function *in vivo*. Human DJ-1 was previously found to respond to oxidative stress (8). This finding prompted us to analyze the response of *DJ-1A RNAi* flies under oxidative conditions. We used the *elav*-GAL4 driver to systematically induce DJ-1A RNAi in postmitotic neurons of transgenic flies and examined the response of these flies to treatment with exogenous H_2O_2. When treated with 1% H_2O_2, the time to reach 50% mortality was shortened by 27% in *DJ-1A RNAi* flies than control flies (Fig. 3*A*). This finding suggests that neuronal DJ-1A is important in fending off H_2O_2-induced lethality. To further confirm the sensitivity of *DJ-1A RNAi* flies to intracellular H_2O_2 levels, we treated DJ-1A RNAi flies with 3-AT, a known inhibitor of catalase, which converts H_2O_2 to H_2O. DJ-1A RNAi flies were found to be more sensitive to 3-AT treatment than the control flies (Fig. 3*B*). To test whether DJ-1A may be actively involved in ROS scavenging, we also overexpressed DJ-1A ubiquitously with the Da-GAL4 driver and observed that DJ-1A overexpression was sufficient to confer resistance against 3-AT treatment (Fig. 6, which is published as supporting information on the PNAS web site).

If DJ-1A normally plays a critical role in sensing cellular ROS levels and eliciting protective responses to remove these toxic agents, one would predict that inhibiting DJ-1A function would lead to elevated levels of endogenous ROS. We tested this possibility by staining cultured neurons with DCFH-DA, which is an indicator of hydroxyl free radicals. Compared with control neuronal culture,